Computers and Concrete, *Vol. 24, No. 4 (2019) 379-397*
DOI: https://doi.org/10.12989/cac.2019.24.4.379

Statistical bias indicators for the long-term displacement of steel-concrete composite beams

Julian A. Moreno[a], Jorge L.P. Tamayo*, Inácio B. Morsch[b], Marcela P. Miranda and Lucas H. Reginato

Departament of Civil Engineering, Engineering School, Federal University of Rio Grande do Sul, Av. Osvaldo Aranha 99-3o Floor, 90035-190, Porto Alegre, RS, Brazil

(*Received November 23, 2018, Revised September 4, 2019, Accepted September 16, 2019*)

Abstract. Steel-concrete composite beams are widely employed in constructions and their performance at the serviceability stage is of concern among practitioners and design regulations. In this context, an accurate evaluation of long-term deflections via various rheological concrete models is needed. In this work, the performance and predict capability of some concrete creep and shrinkage models ACI, CEB, B3, FIB and GL2000 are ascertained, and compared by using statistical bias indicators. Ten steel-concrete composite beams with existing experimental and numerical results are then modeled for this purpose. The proposed modeling technique uses the finite element method, where the concrete slab and steel beam are modeled with shell finite elements. Concrete is considered as an aging viscoelastic material and cracking is treated with the common smeared approach. The results show that when the experimental ultimate shrinkage strain is used for calibration, all studied rheological models predict nearly similar deflections, which agree with the experimental data. In contrast, significance differences are encountered for some models, when none calibration is made prior to. A value between twenty and thirty times the cracking strain is recommended for the ultimate tensile strain in the tension stiffening model. Also, increasing the relative humidity and decreasing the ambient temperature can lead to a substantial reduction of slab cracking for beams under negative flexure. Finally, there is not a unique rheological model that clearly excels in all scenarios.

Keywords: statistical bias indicators; composite beams; displacement; finite elements; creep and shrinkage

1. Introduction

Nowadays the use of steel-concrete composite beams has spread over the world for the construction of civil engineering structures such as bridges and floors in multistory buildings. There exist various standards in which design guidelines are provided to protect these structures at the serviceability stage, where control of deflections becomes an essential part of the design process. As well known, time-dependent effects and concrete cracking have a meaningful effect on the internal redistribution of stresses at reinforced concrete (RC) sections. In fact, these features are associated to the increase of deflections with time (Nguyen and Hjiaj 2016). In this scenario, it is desirable to undertake an accurate prediction of deflections along the entirely serviceability stage at which the structure is exposed. This may be accomplished via a finite element (FE) based model and viscoelasticity theory, together with a rheological concrete model. Among the most recognized creep and shrinkage models found in the literature, it can be cited the ACI Committee 209 (2008), B3 (Bazant and Bajewa 1995), GL2000 (Gadner and Lockman 2001), CEB MC 90 (CEB 1993), CEB MC 99 (CEB 1999) and FIB 2010 (FIB 2012) models, all of which are developed according to curve fitting procedures of experimental data in concrete specimens, with exception of the B3 model, which has a more rigorous theoretical background. In this study, all the aforementioned models are applied in the evaluation of long-term deflections in composite beams.

The evaluation of long-term deflections in steel-concrete composite beams is of importance and has been topic of various research studies. In Nguyen and Hjiaj (2016), the B3 model is used to evaluate the long-term response of two continuous steel-concrete composite beams for a period of 340 days. Concrete cracking and shrinkage are identified as the major factors for time effects. In Zhu and Su (2017), four simply supported steel-concrete composite beams are modeled with the CEB MC 90, in which good agreement was found between predicted and experimental data. In Ban *et al*. (2015) is studied the long-term behavior of simply supported composite beams with blind bolts, using Australian standards for a period of 260 days. In Erkmen and Bradford (2011) and Liu *et al*. (2013), a long-term analysis based on the CEB model code is carried out for evaluating deflections in simply supported composite beams curved in plan. In Partov and Kantchev (2011) is studied the creep effect in steel-concrete composite beams according to the ACI Committee 209 and CEB MC 90-99 regulations, whilst stochastic analyses are studied in Xiang *et al*. (2016) to account for uncertainties in materials by using the CEB MC 90. In Varshney *et al.* (2013), the CEB MC 90-99 are

*Corresponding author, Professor
E-mail: jorge.tamayo@ufrgs.br
[a]Ph.D.
E-mail: julianavila@ufrgs.br
[b]Ph.D.
E-mail: morsch@ufrgs.br

Copyright © 2019 Techno-Press, Ltd.

ISSN: 1598-8198 (Print), 1598-818X (Online)

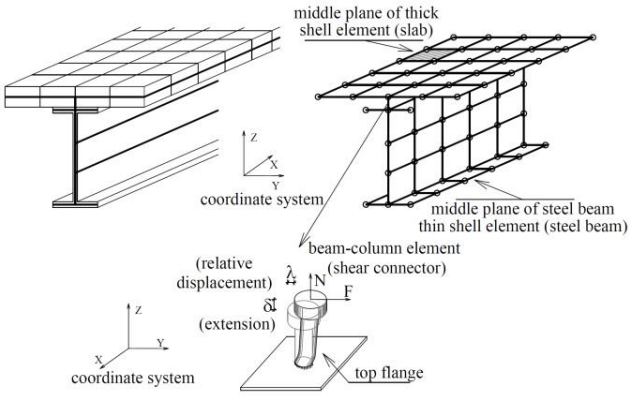

Fig. 1 FE modeling of composite beams by means of shell and beam-column elements

used to assess time effects in composite beams, while in Sousa *et al.* (2013), the long-term response of a pre-stressed concrete bridge, which was monitored for 2000 days, is presented. Thereby, measured data is compared with the long-term numerical predictions using the European standard EC2 (2004). In Gilbert *et al*. (2012), a procedure is presented for the time-dependent service analysis of composite concrete slabs with wave form steel decking, mainly caused by concrete shrinkage.

Other works are based only on the evaluation of creep and shrinkage models in concrete specimens. In Theiner *et al.* (2014), drying shrinkage is assessed via various shrinkage models. In Wendner *et al*. (2015), the performance of a new version of the B3 model, named B4, is evaluated with a huge concrete experimental data set, and also with other model codes such as ACI Committee 209, GL2000 and CEB MC 90-99. In Bazant and Li (2008), statistical bias indicators are used for evaluating the performance of rheological models GL2000, B3, ACI and CEB against laboratory test data. However, works advocated to the comparison of predicted long-term deflections with experimental data in steel-concrete composite beams by using statistical bias indicators for various creep and shrinkage models are more limited, if any. In this work, the aforementioned model codes are selected and their performances are evaluated via five statistical indicators according to the ACI Committee 209 (2008), all of which can measure dispersion between predicted and experimental response along time. In this sense, a better insight can be given about the suitability of each rheological model at the particular case. Otherwise, the used FE model is referred to an in-house code previously developed by the authors (Tamayo *et al.* 2015 and Dias *et al*. 2015), which has proved to perform well against other existing numerical and experimental results (e.g., Reginato *et al.* 2018, Moscoso *et al.* 2017, Tamayo and Awruch 2016). The overall model is fully three-dimensional and is based on shell finite elements, where partial interaction at the slab-beam interface is modeled via bar elements as shown in Fig. 1. Ten steel-concrete composite beams with experimental results are then simulated and corresponding statistical bias indicators for deflections are calculated in all cases.

2. Numerical modeling and constitutive models

At the serviceability limit stage, both steel in tension and compression and concrete in compression behave nearly linearly elastic and nonlinearities are mainly due to concrete cracking and slipping at the slab-beam interface. Concrete is considered to be elastic in tension until its tensile strength is reached along the maximum principal stress direction, and then a crack is form perpendicular to this direction. Cracked concrete then behaves like an orthotropic material following their principal stress directions, where two mutually perpendicular cracks are allowed to form at each monitored point. Concrete in tension between cracks is capable of resisting some tensile stresses as a result of bond action between steel bars and concrete, thus contributing to the overall stiffness of the member, and reducing its deflection. This phenomenon is called tension stiffening and its assessment is relevant for serviceability analyses. Then, a smeared crack approach is assumed to represent discontinuous macrocrack brittle behavior, where initially open cracks can close and reopen due to internal stress redistribution. In this manner, averaged stresses and strains are introduced to predict member behavior.

As it may be expected, concrete cracking has a major role on the long-term response of RC members under service loads (Xu *et al.* 2018). In Fig. 2(a) is depicted the stress-strain relationship available in the current FE code for cracked concrete due to tension stiffening and tension softening. In these diagrams, $\propto \approx$ 0.5-0.7, f_t is the tensile concrete strength, ε_{cr} is the cracking strain, ε_{tu} is the ultimate tensile strain and E_c is the Young modulus of the material. In this work, it is considered that the tension stiffening diagram also accounts for the tension softening of cracked concrete and bond slip effects (Baskar *et al.* 2002). Regular concrete modeling defines mesh objectivity of FE results based on the fracture energy of brittle materials, G_f, and associated element size, h (Dias *et al.* 2015). In this sense, the ultimate tensile strain can be determined. Nevertheless, RC slabs in steel-concrete composite beams deserve special attention as their behavior may not be modeled with regular concrete modeling in FE analyses, and some calibration may be needed for defining ε_{tu} at the particular problem (see e.g., Baskar *et al.* 2002, Ramnavas *et al.* 2015, Reginato *et al.* 2018, ABAQUS 2011). For instance, a value of 0.001 seems reasonable for heavily reinforced concrete, while in other situations typical values around $\varepsilon_{tu} \cong (10-20)\varepsilon_{cr}$ for common RC slabs are suggested by some researches (Baskar *et al*. 2002, Damjanic and Owen 1984). In contrast, a much higher value of 0.1 is recommended for concrete slabs acting in composite beams (Liang *et al.* 2005, Baskar *et al.* 2002, Rex and Easterling 2000). The trouble in defining ε_{tu} lies in the fact that the RC slab failure due to concrete cracking in tension or compression does not imply overall failure of the structure, as the steel beam is able to resist additional load. Therefore, it seems to be arguable to adopt a random preliminary value, so a calibration procedure has been preferred in this study. After various trial analyses, values in the range of $\varepsilon_{tu} = (20-30)\varepsilon_{cr}$ have better fit the current

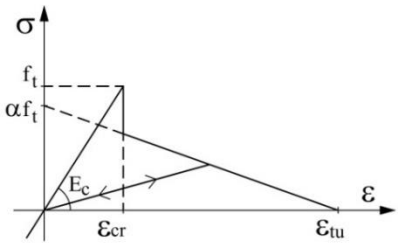

(a) One-dimensional behavior in tension

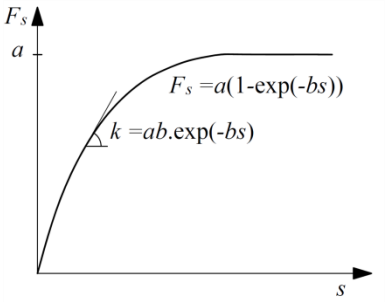

(b) Shear force versus slip

Fig. 2 Constitutive laws

experimental data for the studied examples, then as a starting point, a value around $25\,\varepsilon_{cr}$ is recommended herein. In relation to the long-term performance, concrete is treated regularly as a viscoelastic ageing material whose mechanism is commented in section 2.1. Otherwise, the steel beam behaves linearly elastic under service loads.

Shell elements with eight and four nodes are used to represent the middle planes of the RC slab and parts of the steel beam, respectively. The RC slab is composed of several layers through its thickness to capture nonlinear concrete behavior, where additional smeared layers are used to represent reinforcing bars. The gap equal to the sum of half slab thickness plus half top flange thickness exists between the slab and the top steel flange of the beam. Therefore, a special beam-column element of length equal to this gap joints adjacent nodes of the middle-plane of the slab and that of the top steel flange at discrete locations. Strictly speaking, there is no geometric contact between these surfaces as already shown in Fig. 1. The interaction is accomplished by connectors disposed along the longitudinal direction of the beam in which uplift is not permitted by employing a great axial stiffness in the connector element, while compatibility of rotations are enforced in adjacent nodes of the steel and slab based on the assumption that the beam section remains plane after deformation. The relative displacement in the sliding direction at the interface is computed based on the connector end displacements and rotation. The shear stiffness along the sliding direction is the slope of the shear-slip relationship displayed in Fig. 2(b), in which F_s is the shear force in the connector, s the associated slip and a,b model parameters. When the space between connectors is considerable in the real project, fictitious elements with great axial stiffness can be introduced to avoid surface interpenetration (Tamayo *et al*. 2019). Based on a mesh sensitivity assessment, three meshes are considered for each composite beam. For instance, Fig. 3 depicts the three meshes used in the case of

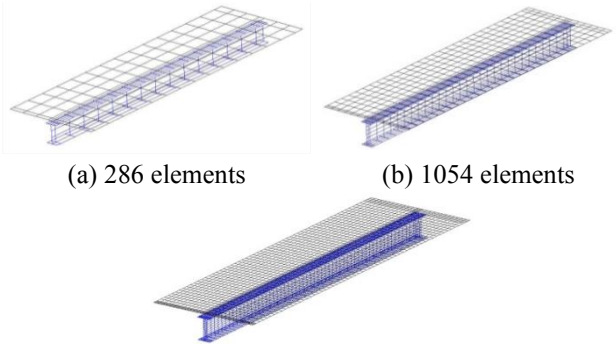

(a) 286 elements (b) 1054 elements

(c) 4126 elements

Fig. 3 FE meshes for simply supported composite beam B1

beam B1 of section 4.1. The coarser mesh in Fig. 3(a) yields similar results to the other ones, then this mesh is used in the following computations.

2.1 Solidification theory for concrete creep

The deformational behavior of concrete can be described mathematically as the sum of the short- and the long-term behavior of the material. Accordingly, the total strain $\varepsilon_T(t)$ at time t can be decomposed as follows

$$\varepsilon_T(t) = \varepsilon_i(t) + \varepsilon_v(t) + \varepsilon_{sh}(t) \tag{1}$$

where $\varepsilon_T(t)$, $\varepsilon_v(t)$ and $\varepsilon_{sh}(t)$ are the instantaneous part of the stress-dependent strains, viscoelastic and shrinkage strains, respectively. The uniaxial constitutive relation defining concrete as an ageing viscoelastic material with the instantaneous plus the viscoelastic parts under a stress history is introduced by the Stieltjes integral, which also applies to discontinuous functions.

$$\varepsilon_\sigma(t) = \int_0^t J(t,t')\partial\sigma(t') \tag{2}$$

in which $J(t,t')$ is the compliance function for a constant stress applied at time t'. The preceding integral-type constitutive equation can be converted to a differential-type form consisting of a system of first-order ordinary differential equation by using Dirichlet series expansion. Indeed, Solidification Theory (Bazant and Prasannan 1989) uses a rate-type creep law based on a Kelvin model with non-ageing properties for representing the microstrain $\gamma(t)$ of the solidified matter (i.e., hydrated cement) as stated in Eq. (3).

$$\eta_\mu \dot{\gamma}_\mu + E_\mu \gamma_\mu = \sigma, \qquad \gamma = \sum_{\mu=1}^{N} \gamma_\mu \tag{3}$$

Integration of Eq. (3) for a constant unit stress σ applied at age t' yields

$$\gamma(t-t') = \sum_{\mu=1}^{N} \frac{1}{E_\mu}(1-e^{-(t-t')/\tau_\mu}), \qquad \tau_\mu = \eta_\mu / E_\mu \tag{4}$$

where E_μ, τ_μ and η_μ are the elastic modulus, retardation time and viscosity of the μ-th Kelvin unit, respectively and N is the total number of units in the chain. Moreover, the

compliance function according to the Solidification theory can be expressed by Eq. (5).

$$J(t,t') = \frac{1}{E_0} + \frac{\gamma(t-t')}{\upsilon(t)} \tag{5}$$

where E_0 is the modulus of elasticity for the aggregates and microscopic particles of the cement paste.

This form renders compliance functions given in some design regulations so that time-dependent functions, i.e., volume fraction of the solidified matter, $\upsilon(t)$, and $\gamma(t-t')$ can be identified. In this manner, parameters E_μ may be determined from Eq. (4) by the method of least squares. To permit structural creep analysis with increasing time, Eq. (3) is resolved with an exponential algorithm by considering that σ varies linearly during a time step i. The corresponding microstrain increment between times t_i and t_{i+1} is then given by Eq. (6).

$$\Delta\gamma = \gamma_{i+1} - \gamma_i = \Delta\sigma \sum_{\mu=1}^{N} \left(\frac{1-\lambda_\mu}{E_\mu} \right) + \sum_{\mu=1}^{N} \left(\frac{\sigma_i}{E_\mu} - \gamma_{\mu_i} \right) \left(1 - e^{-\Delta y_\mu} \right) \tag{6}$$

For $\varepsilon(t)$, the quasi-elastic stress-strain relation is obtained in Eq. (7) by using $\Delta\varepsilon = \Delta\sigma / E_{i+1/2} + \Delta\gamma / \upsilon_{i+1/2} + \Delta\varepsilon_{sh}$ and $\Delta\sigma = \sigma_{i+1} - \sigma_i$.

$$\Delta\sigma = E^* (\Delta\varepsilon - \Delta\varepsilon^*) \tag{7}$$

where parameters Δy_μ, λ_μ, E^* and $\Delta\varepsilon^*$ are given in section 2.3 for the three-dimensional case. Then, the rheological problem can be treated as a quasi-elastic analysis with initial strains as will be explained in section 2.2. Moreover, concrete is considered as an aging viscoelastic linear material in compression under the elastic limit and in tension before cracking. It is further assumed that the principle of superposition is still valid in the cracked phase, where the creep phenomenon is coupled to the behavior due to tension stiffening effect. A smeared fixed crack approach is used to model the behavior of cracked concrete, coupled with a tensile strength criterion to predict crack initiation. Two orthogonal cracked planes are allowed to form at each sampling point and a reduced shear modulus is used in the cracked zones. Full bond is assumed at the concrete/reinforced interface, but the tension stiffening concept is used to account for the gradual bond deterioration with progressive cracking (Tamayo *et al*. 2015). The creep compliance function and the shrinkage strains are also assumed to be the same in tension and compression (Macorini *et al*. 2006, Sakr and Sakla 2008).

2.2 Numerical simulation procedure

The entire time period is divided into a number of time steps Δt_1, Δt_2, Δt_3,…, Δt_n, in which changes in external loads occur at the beginning of a time step. The external load may be further subdivided into a number of load steps as shown in Fig. 4. The procedure is summarized as follows.

1. Read the load control data for the current time t_i and time step $\Delta t_1(\Delta t_1 = t_{i+1} - t_i)$. Form the applied load vector $R(t_i)$ for time t_i. Divide this vector according to a given number of load steps to obtain the load vector for each load step of the current increment.

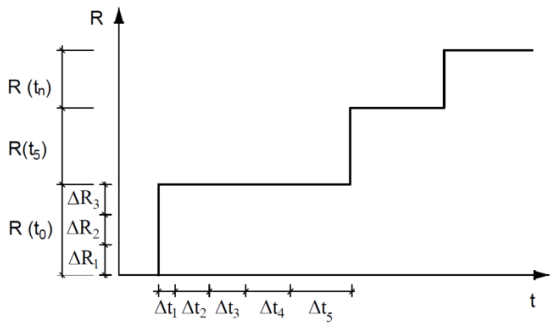

(a) Load history

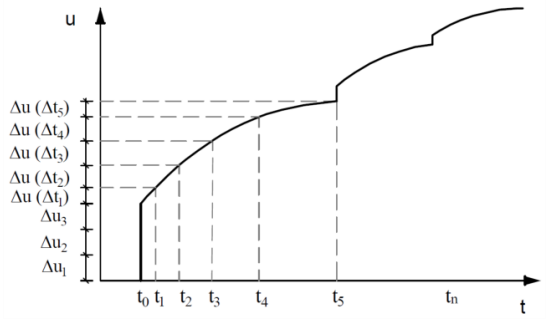

(b) Long-term displacement

Fig. 4 History of applied loads and computed displacements

2. Start iterative solutions procedure for this load step.
3. Form the element stiffness matrices, and assemble the structural stiffness matrix.
4. Solve the equilibrium equations to obtain nodal displacements increment vector. Add this to the previous ones to obtain the current total nodal displacement vector
5. For each element calculate the displacement, strain and stress increments. Update material matrix, and calculate the element resisting forces based on the current state. The stress increment vector is obtained through the material constitutive matrix and the mechanical strains.
6. Assemble the unbalanced force vector, which is given by subtracting the total applied external load from the internal resisting force vector. Check the force convergence.
7. If convergence has not been obtained, go back to step 3 and repeat steps 3 through 6 until convergence is achieved. Continue to step 8, or if the solution diverges, stop the calculations.
8. If this is not the last load step for the current time, go back to step 1 and repeat steps 1 to 7 until the solution is obtained for all the specified load steps. When the last load step was reached, go to step 9.
9. Calculate the material properties at the end of the time steps, i.e., for time t_{i+1}. For each element the creep and shrinkage strains are calculated. The equivalent nodal loads for each element are calculated by considering these strains as initial strains (see section 2.3) and then they are assembled into the load increment vector $\{\Delta R\}_i$. Go to step 1 and repeat steps 1 to 7.
10. If time t_i is the last time the analysis is finished, otherwise go back to step 1 and continue the analysis for the next time step.

Table 1 Parameters ranges of concrete creep and shrinkage models

Input variables	ACI 209	B3	CEB MC 90	CEB MC 99	GL2000	FIB2010
f_{cm},28 (MPa)	---	17 to 70	20 to 90	15 to 120	16 to 82	20 to 130
a/c	---	2.5 to 13.5	---	---	---	
Cement content (kg/m^3)	279 to 446	160 to 720	---	---	---	---
w/c	---	0.35 to 0.85	---	---	0.40 to 0.60	
Relative humidity, %	40 to 100	40 to 100	40 to 100	40 to 100	20 to 100	40 to 100
Type of cement (U.S.)	I or III	I,II,III	I,II,III	I,II,III	I,II,III	I,II,III
t_c (moist cured)	≥1 day	≥1 day	<14 days	<14 days	≥1 day	<14 days
t_c (steam cured)	1 to 3 days	---	---	---	---	
t_o (age at loading)	≥7 day	$t_o \geq t_c$	>1 day	>1 day	$t_o \geq t_c \geq 1$ day	>1 day
Temperature (^{o}C)	---	---	5 to 30	10 to 30	---	5 to 30

2.3 Solution procedure for creep and shrinkage effects

At the beginning of the time step *i*, ($\Delta t_1=t_{i+1}-t_i$), the stress vector $\{\sigma\}_i$ is known, as well as the stress vector $\{\sigma\}_{i-1}$ of the previous step. The stress increment vector for time step *i* is calculated with $\{\Delta\sigma\}_i=\{\sigma\}_i-\{\sigma\}_{i-1}$. For the first time step, $\{\Delta\sigma\}_{i-1}$ is set to zero.

The following algorithm is used for calculating equivalent nodal forces due to long-term effects:

- For e=1… m (where m is the total number of finite elements in the concrete slab);
- For g=1… p (where p is the total number of sampling points for all layers):

1. The shrinkage strain increment is in the current step given by:

$$\{\Delta\varepsilon_{sh}\}_{(g,e,i)} = \{\varepsilon_{sh}\}_{(g,e,i+1)} - \{\varepsilon_{sh}\}_{(g,e,i)}$$

2. Total strain increment due to creep and shrinkage is then computed by:

$$\{\Delta\varepsilon^*\}_{(g,e,i)} = \sum_{\mu=1}^{N} \{\varepsilon^*\}_{(g,e,i)} (1-e^{-\Delta y_\mu}) + \{\Delta\varepsilon_{sh}\}_{(g,e,i)}$$

$$\{\varepsilon_\mu{}^*\}_{(g,e,i)} = [D_\mu]^{-1}_{(g,e,i)} \{\Delta\sigma\}_{(g,e,i)} + \{\varepsilon_\mu{}^*\}_{(g,e,i-1)} (e^{-\Delta y_\mu})$$

where $[D_\mu]^{-1}$ is the compliance constitutive matrix evaluated with an elasticity modulus equal to E_μ $\upsilon_{i+1/2}/\lambda_\mu$ with $\lambda_\mu = (1-e^{\Delta y_\mu})/\Delta y_\mu$ and $\Delta y_\mu = \Delta t_i / \tau_\mu$, where i+1/2 refers to the middle of the interval [t_i, t_{i+1}]. It can be noted that it is necessary to store only the viscous strain of the previous step, avoiding storing all the loading history. Note that the total strain increment can be evaluated before the solution of the time step begins.

3. Matrix $[D]^*$ is evaluated by:

$$[D]^* = \begin{bmatrix} \frac{E^*}{1-\nu^2} & \frac{\nu E^*}{1-\nu^2} & 0 & 0 & 0 \\ \frac{\nu E^*}{1-\nu^2} & \frac{E^*}{1-\nu^2} & 0 & 0 & 0 \\ 0 & 0 & \beta G & 0 & 0 \\ 0 & 0 & 0 & \beta G & 0 \\ 0 & 0 & 0 & 0 & \beta G \end{bmatrix}$$

$$\frac{1}{E^*} = \frac{1}{E_{i+1/2}} + \sum_{\mu=1}^{N} \frac{1-\lambda_\mu}{E_\mu \upsilon_{i+1/2}}$$

with $G=E^*/2(1+\nu)$ and ν is the coefficient of Poisson and β is the shear retention factor for cracked concrete. The normal stress perpendicular to the slab middle plane is disconsidered.

4. The equivalent element force vector is formed by summation of the contribution of each sampling point:

$$\{\Delta R\}_{(e,i)} = \sum_{g=1}^{p} \int_{V_e} [B]^T_{(g,e)} [D]^*_{(g,e,i)} \{\Delta\varepsilon^*\}_{(g,e,i)} dV_e$$

5. The global force vector due to creep and shrinkage at time step *i*, $\{\Delta R\}_i$, is assembled, considering the contribution of each load vector at the element level.

3. Statistical bias indicators

Various creep and shrinkage models are proposed in the technical literature to predict concrete long-term response with different number of input parameters as shown in Table 1. It is crucial to have the best estimate of deflections not only at the end of the analysis, but for the entirely stress history of the structure. To compare the accuracy of each model in relation to laboratory test data of ten steel-concrete composite beams, five statistic indicators are used. The advantages of each statistical indicator are best explained in the following sections, but they are weighted depending on the time interval at which more test data is available. Indeed, concrete creep and shrinkage have a more pronounced effect during the first months, and their effects decrease as time progresses. In this manner, it is expected that common measured data will be more grouped at early times.

3.1 Normalized standard deviation for experimental points

In a first approach, the standard deviation (*SD*) expressed in Eq. (8) is calculated at time stations where experimental data is available. To make all results dimensionless, a coefficient of relative difference, namely RD_{EXP}, is introduced in Eq. (9).

$$SD = \sqrt{\frac{\sum_{i=1}^{n} (C_i - O_i)^2}{n}} \tag{8}$$

$$RD_{EXP} = \sqrt{\frac{1}{n}.\sum_{i=1}^{n} RD_i^2} \tag{9}$$

$$RD_i = \frac{(C_i - O_i)}{O_i} \tag{10}$$

where n is the number of observed points, O_i and C_i are the i-th measured and i-th predicted value of the variable in question (i.e., deflections), and RD_i is the normalized difference between these two points. One problem with conventional statistical indicators is the increasing divergence and scatter, so for common techniques such linear regression or percent deviation, the weighting of the later data could be greater than that of the earlier data or viceversa, therefore these techniques may not be adequate to uniquely distinguish between models. In an attempt to minimize this bias, a second approach, namely $RD100_p$, is employed. This consists in defining points equally spaced at even time intervals in Eq. (9). e.g., n=100. Thereafter, a linear interpolation technique is applied to determine new "experimental" points, which are in charge of suppressing part of the scatter data. However, an inherent error is unavoidably introduced due to data manipulation. Thus, these coefficients are only taken as a reference because they are not a good measure of dispersion.

3.2 The BP coefficient of variation ω_{BP}

A coefficient of variation ω_{BP} (Bazant and Panula 1978) is determined for each data set, which is defined as the group of points contained in each logarithmic decade, 0 to 9.9 days, 10 to 99.9 days, and so on. A weight is then assigned to each point based on the decade it belongs to and number of points contained in that decade. The coefficient of variation for all data sets is the root mean square of the data set values as stated in Eq. (11).

$$\omega_{BP} = \sqrt{\frac{1}{N}\sum_{j=1}^{N} \omega_j^{\,2}} \tag{11}$$

$$\omega_j = \frac{1}{\overline{O}_j}\sqrt{\frac{1}{n-1}.\sum_{i=1}^{n} \omega_{ij}\left(C_{ij} - O_{ij}\right)^2} \tag{12}$$

$$\overline{O}_j = \frac{1}{n_w}\sum_{i=1}^{n} \omega_{ij} O_{ij} \tag{13}$$

$$\omega_{ij} = \frac{n}{n_d n_k} \tag{14}$$

where n is the number of data points in data set number j, n_w is the sum of the weights of all data points in a data set, n_k is the number of data points in the k-th decade, n_d is the number of decades on the logarithmic scale spanned by measured data in data set j, N is the number of data sets, O_{ij} and C_{ij} are the measured and predicted values of deflection, respectively, for the i-th data point in data set number j, ω_{ij} is the weight attributed to the i-th data point in data set number j, ω_j is the coefficient of variation for data set number j and ω_{BP} is the overall coefficient of variation. The weight assigned to a data point in a decade on the logarithm scale is taken as inversely proportional to the number of data points, n_k in that decade. The weights are normalized such that their sum equals to 1.0.

3.3 CEB Statistical indicators: V_{CEB}, F_{CEB} and M_{CEB}

The CEB statistical indicators are the coefficient of variation V_{CEB}, the mean square error F_{CEB} and the mean deviation M_{CEB} (Muller and Hilsforf 1990). These three indicators are evaluated in six time ranges of 0 to 10 days, 11 to 100 days, 101 to 365 days, 366 to 730 days, 731 to 1095 days, and above 1095 days. The final values are the root mean square of the six internal values. The CEB coefficient of variation is calculated with the following expression

$$V_{CEB} = \sqrt{\frac{1}{N}\sum_{j=1}^{N} V_j^{\,2}} \tag{15}$$

$$V_j = \frac{1}{\overline{O}_j}\sqrt{\frac{1}{n-1}.\sum_{i=1}^{n} \left(C_{ij} - O_{ij}\right)^2} \tag{16}$$

$$\overline{O}_j = \frac{1}{n}\sum_{i=1}^{n} O_{ij} \tag{17}$$

where n is the number of data points in interval j, N is the total number of data sets considered, and V_j is the coefficient of variation in interval j. Otherwise, the CEB mean square error is determined with the following expressions:

$$F_{CEB} = \sqrt{\frac{1}{N}\sum_{j=1}^{N} F_j^{\,2}} \tag{18}$$

$$F_j = \sqrt{\frac{1}{n-1}.\sum_{i=1}^{n} f_i^{\,2}} \tag{19}$$

$$f_i = \frac{(C_{ij} - O_{ij})}{O_{ij}} \times 100 \tag{20}$$

where f_i is the percentage difference between calculated and observed data point i and F_j is the mean square error in interval j. Finally, the CEB mean deviation indicates systematic overestimation or underestimation of a given model with the following expression

$$M_{CEB} = \frac{\sum_{j=1}^{N} M_j}{N} \tag{21}$$

$$M_j = \frac{1}{n}\sum_{i=1}^{n} \frac{C_{ij}}{O_{ij}} \tag{22}$$

where M_j is the ratio of calculated to experimental values in time range j. Other variables not mentioned above have the same meaning as in the previous sections.

3.4 The Gardner coefficient of variation ω_G

A not common definition of coefficient of variation is proposed by Gardner (2004), the mean observed value and the root mean square of the difference between calculated and

observed values are calculated in half logarithmic time intervals: 3 to 9.9 days, 10 to 31.5 days, 31.6 to 99 days, 100 to 315 days, 316 to 999 days, 1000 to 3159 days, and above 3160 days. The duration of each time interval is 3.16 times the previous one. To obtain a criterion of fit, the average values and root mean squares are averaged without regard to the number of observations in each half-decade. Then, the coefficient of variation is obtained by dividing the average root mean square normalized by the average value.

$$\omega_G = \frac{\overline{RMS}}{\overline{O}} \tag{23}$$

$$\overline{RMS} = \frac{1}{N}\sum_{j=1}^{n} RMS_j \tag{24}$$

$$RMS_j = \sqrt{\frac{1}{n-1}.\sum_{i=1}^{n}\left(C_{ij} - O_{ij}\right)^2} \tag{25}$$

$$\overline{O} = \frac{1}{N}\sum_{j=1}^{n}\overline{O}_j \tag{26}$$

$$\overline{O}_j = \frac{1}{n}\sum_{i=1}^{n} O_{ij} \tag{27}$$

For all aforementioned indicators, a perfect correlation means 0%, while this is 1.0 for the M_{CEB} indicator. That is, values greater and less than 1.0 indicate overestimation and underestimation, respectively.

4. Numerical applications

Environmental conditions such as temperature and relative humidity at which experimental tests were performed are not reported in six of the ten beams studied here (section 4.1 and 4.2), but creep and shrinkage strain evolutions, which were obtained by means of separated cylindrical specimens, are available or at least the ultimate values are given. In these cases, a curve fitting or adjusting procedure is used, i.e. mean values for the environmental humidity, temperature, and cement type of the mix are initially adopted based on the recommendations given in Table 1. If the ultimate shrinkage is not achieved with this initial data set, another set of parameters is chosen and the procedure is repeated until finally achieve the given ultimate shrinkage strain. Meanwhile, the construction sequences, curing time and external loads are kept constant in all simulations. Emphasis is given to the shrinkage calibration because it has a major effect in the evaluation of deflections in relation to creep for the studied examples (Gilbert *et al.* 2012, Gilbert and Bradford 1995, Jiang *et al.* 2009, Wang *et al.* 2011, Jurkiewiez *et al.* 2005). Only the composite beams tested by Fan *et al*. (2010) in section 4.3 have all environmental data available. Then, a non-calibrated analysis with the current environmental data is additionally realized for these beams. A detail description of the adopted material properties can be found in the work of Moreno (2016).

According to the experimental reports, all tested beams are propped after casting of the slab, and they remain in this situation up to the age of loading, after which the props were moved and the composite beam allowed deforming due to shrinkage and external load. Also, the use of wet curing and testing at early age minimizes early shrinkage effects at this pre-loading stage (Bischoff 2001, Bradford 1997). Thus, the effect of shrinkage, up to the time of the props are present, would be negligible. Therefore, for the numerical simulations the time-history analysis commences at the age of loading, in which creep, shrinkage and cracking commence to act together over the composite section. In section 4.4, a parametric study is carried out to assess the effect of tension stiffening by means of the ultimate tensile strain, relative humidity and temperature on the computed long-term displacements. Finally in section 4.5, a practical example of a girder bridge is presented by using unpropped construction and considering a pre-loading stage (Kaklauskas *et al*. 2009).

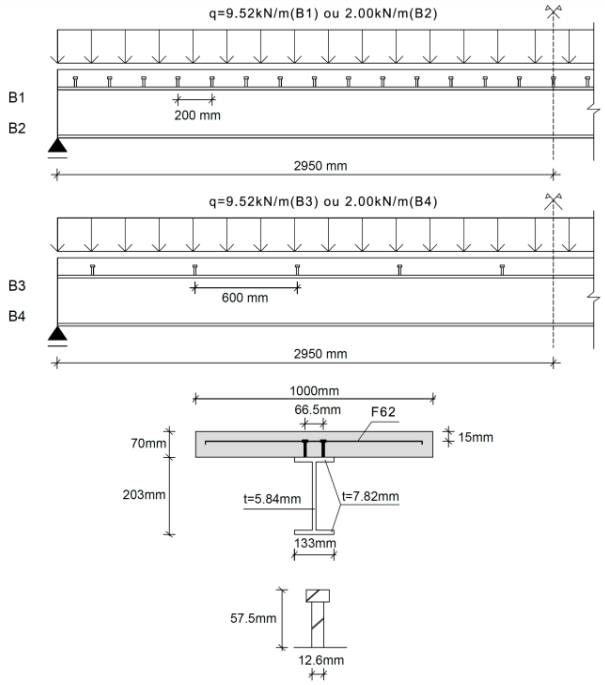

Fig. 5 Geometry and cross-section of beams B1,B2,B3 and B4

4.1 Simply supported steel-concrete composite beams tested by Bradford and Gilbert (1991)

Four simply supported steel-concrete composite beams, namely B1, B2, B3 and B4, were tested by Bradford and Gilbert (1991) under sustained uniform vertical loads. All beam specimens are subjected to their self-weight (1.92 kN/m), but beams B1 and B3 carried out an additional load of 7.52 kN/m. The loads are applied at 10 days after concrete casting and thereafter they are sustained for a period of 250 days. In Fig. 5 are depicted the geometry and cross sections of the beams, where pairs of connectors are welded to the top flange at 200 mm and 600 mm intervals for beams B1, B2 and B3, B4, respectively. The concrete compressive strength is 31 MPa, the ultimate shrinkage strain reported in the experimental work is 415×10^{-6} and the creep coefficient at the end of the analysis is 2.60. Other data sets related to environmental conditions during the test are not informed, and then typical values are assumed (see

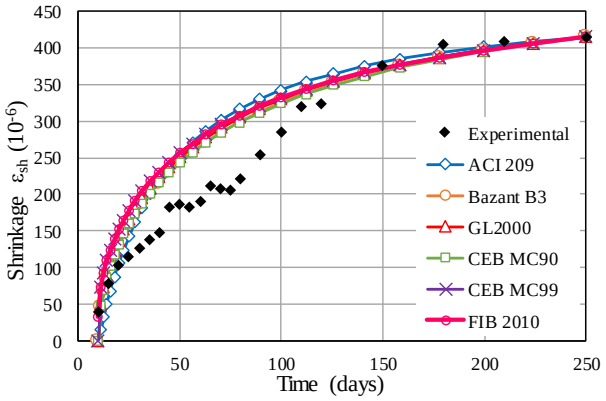

Fig. 6 Curve fitting for ultimate shrinkage strain

Table 2 Statistical indicator for deflection at mid-span in beam B1

Model	RD_{EXP} (%)	RD_{100p} (%)	ω_{BP} (%)	V_{CEB} (%)	F_{CEB} (%)	M_{CEB}	ω_G (%)
ACI 209	3.90	3.88	4.05	4.54	5.38	1.02	5.50
Bazant B3	4.56	4.30	4.75	5.33	6.77	1.02	6.76
GL2000	5.51	4.36	6.20	7.25	8.65	1.05	8.31
CEB MC90	4.35	3.70	4.60	5.31	6.54	1.03	6.44
CEB MC99	4.98	4.33	5.19	5.92	7.38	1.03	7.38
FIB 2010	5.34	4.76	5.50	6.19	7.70	1.02	7.82

Table 3 Statistical indicator for deflection at mid-span in beam B3

Model	RD_{EXP} (%)	RD_{100p} (%)	ω_{BP} (%)	V_{CEB} (%)	F_{CEB} (%)	M_{CEB}	ω_G (%)
ACI 209	5.68	4.99	9.06	6.27	6.60	1.09	6.62
Bazant B3	5.71	4.92	9.54	6.39	7.02	1.10	7.14
GL2000	8.39	7.51	11.23	8.84	9.53	1.12	10.09
CEB MC90	6.43	5.75	9.10	7.00	7.55	1.09	7.88
CEB MC99	6.19	5.33	9.16	7.11	7.80	1.09	7.97
FIB 2010	6.07	5.13	9.16	7.12	7.87	1.09	8.00

Table 1). As commented before, the relative humidity and temperature values are defined according to each rheological concrete model in order to match the ultimate shrinkage strain as depicted in Fig. 6. The slab is reinforced with a steel mesh F62, which is comprised of 6mm longitudinal and cross bars at 200 mm intervals.

The abnormal behavior between 20 and 120 days given in Fig. 6 can be attributed to excessively humid conditions during the experiment, for which the numerical results are not able to capture due to the use of mean values for the environmental humidity and temperature. As it is expected, only the given ultimate shrinkage strain is attained for all models by the fitting procedure. In Figs. 7 and 8 are shown the deflection history at mid-span for beams B1, B2 and B3, B4, respectively, for all studied creep and shrinkage models. The obtained results are also compared with the experimental data and other published results (Wang *et al.* 2010, Jurkiewiez *et al.* 2005 and Giussani and Mola 2010). As it may be observed, good agreement is found for beams B1 and B3, whereas a more significance discrepancy is distinguished for beams B2 and B4, which are subjected to their self-weight only. This mismatch, which may be

Table 4 Statistical indicator for deflection at mid-span in beam B2

Model	RD_{EXP} (%)	RD_{100p} (%)	ω_{BP} (%)	V_{CEB} (%)	F_{CEB} (%)	M_{CEB}	ω_G (%)
ACI 209	15.15	16.04	19.14	12.76	13.38	0.80	15.23
Bazant B3	17.07	18.17	21.74	14.92	14.68	0.78	16.27
GL2000	16.11	17.62	21.55	14.50	14.14	0.79	15.11
CEB MC90	17.39	18.59	22.40	15.24	14.96	0.78	16.43
CEB MC99	15.11	16.81	21.02	13.87	13.44	0.79	13.97
FIB 2010	15.23	16.92	21.15	13.98	13.55	0.79	14.08

Table 5 Statistical indicator for deflection at mid-span in beam B4

Model	RD_{EXP} (%)	RD_{100p} (%)	ω_{BP} (%)	V_{CEB} (%)	F_{CEB} (%)	M_{CEB}	ω_G (%)
ACI 209	20.50	18.85	24.57	16.83	17.92	0.73	19.61
Bazant B3	21.07	20.95	26.35	18.16	17.92	0.73	19.94
GL2000	20.14	20.43	26.23	17.70	17.32	0.74	18.99
CEB MC90	21.37	21.32	27.00	18.44	18.17	0.73	20.15
CEB MC99	19.10	19.69	25.73	16.94	16.34	0.74	17.67
FIB 2010	19.16	19.81	25.84	17.05	16.41	0.74	17.74

considered negligible in practical terms, e.g., 3 mm for the ultimate deflection value, is also corroborated by the results published in the quoted references. Statistical bias indicators are presented in Tables 2 and 3 for beams B1 and B3, respectively. The statistical indicators represent different quantities, and comparisons can only be made across a column, but they cannot be made between columns in tables. In general the coefficients of variations are less than 10% and around 1.0 for the M_{CEB}. As a reference, there exists a recommendation provided by the ACI committee 209 (2008), which is intended for shrinkage strains in concrete specimens, but not for deflections. There, values below 15% and around 20% are considered to be excellent and adequate, respectively. In Tables 4 and 5 are shown the results for beams B2 and B4, respectively. In sum up, the lower percentage differences, i.e., best results are obtained for the ACI model for beams B1, B2, B3 and for the CEB MC 99 and ACI models in the case of beam B4. The associated coefficients of variations for beams B2 and B4 vary between 12.76% and 27.0%, whereas they are below 10% for beams B1 and B3. In general, the FIB 2010 model accompanies the CEB MC99. It is important to mention that RD_{EXP} and RD_{100p} coefficients are merely displayed as reference values because they do not necessarily represent a good measure of dispersion. The best model is appointed based on the partial results at each column of each table. That is, a candidate model is selected with the lowest percentage value for the ω_{BP}, V_{CEB}, F_{CEB} and ω_G indicators or with the closest value to 1.0 in the case of M_{CEB}. Then, the model that better succeed more times is distinguished as the best.

4.2 Continuous steel-concrete composite beams tested by Gilbert and Bradford (1995)

Two-span steel-concrete continuous beams, namely B1 and B2, were tested by Gilbert and Bradford (1995) for a

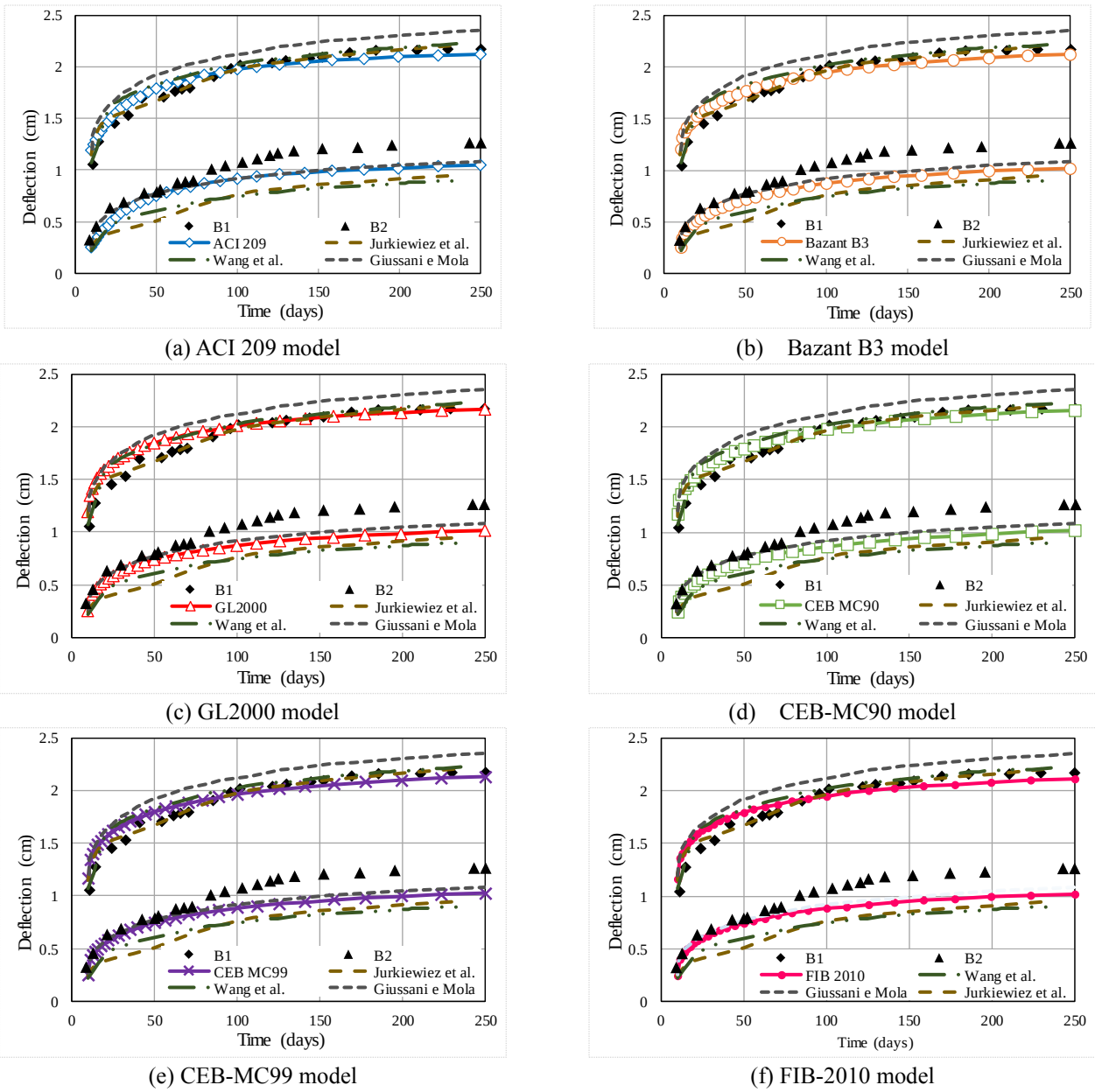

(a) ACI 209 model (b) Bazant B3 model

(c) GL2000 model (d) CEB-MC90 model

(e) CEB-MC99 model (f) FIB-2010 model

Fig. 7 Theoretical and experimental mid-span long-term deflection for beams B1/B2

period of 340 days. Both beams are identical except in the applied load level, details of which are depicted in Fig 9. Beam B1 only supports its own weight (1.92 kN/m), while beam B2 support an additional live load of 4.75 kN/m (6.67 kN/m in total). No arrangement of connectors is given in the experimental report, then shear connectors are designed to be 9 mm in diameter, 50 mm in height, and located in pairs at even intervals of 145 mm (Jiang *et al.* 2009). The age of loading and curing time are adopted as 7 days after concrete casting (Chaudharya *et al.* 2007). The ultimate shrinkage strain and creep coefficient are 520×10^{-6} and 1.68, respectively. Other data set about environmental conditions are not reported, so the aforementioned fitting approach is applied. Concrete compressive strength is 27 MPa. The reinforcement layout in the slab is not indicated in the original reference, only a total longitudinal steel area of 113 mm^2 is reported.

In Fig. 10 are shown the mid-span deflection versus time curves for beams B1 and B2. As it may be observed, the ultimate deflection is slightly overestimated (0.5 mm) for beam B2, whilst it is nearly equal to the experimental value for beam B1. In contrast, a significance difference is encountered for deflection values between 50 and 150 days. Moreover, cracking depends upon each rheological concrete model and can be identified by nearly vertical jumps in the curves. These abrupt changes of slope in the numerical curves are due to cracking that progressively occurs at certain time steps in layers of concrete elements. In Tables 6 and 7 are listed the corresponding coefficient of variations for beams B1 and B2, respectively. The best results are obtained for the B3 and CEB MC 99 models for beam B1, whereas they are the CEB MC 90, FIB2010 and B3 models for beam B2. Conversely, it is interesting to note that the B3 model would be one of the worst models according to

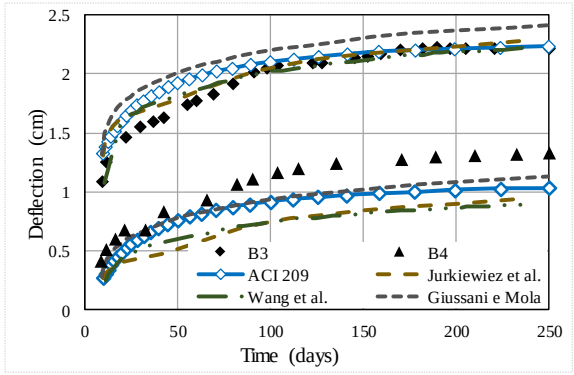

(a) ACI 209 model

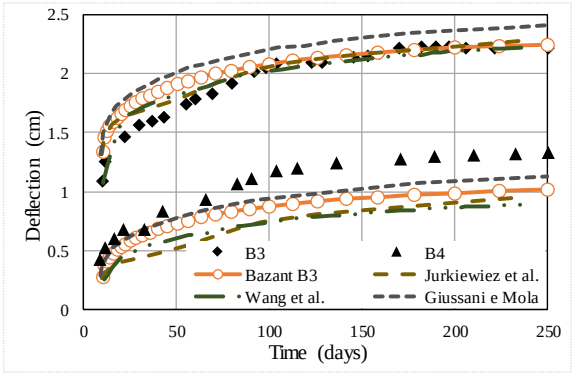

(b) Bazant B3 model

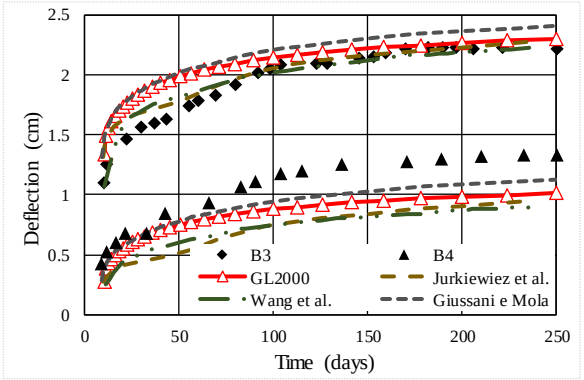

(c) GL 2000 model

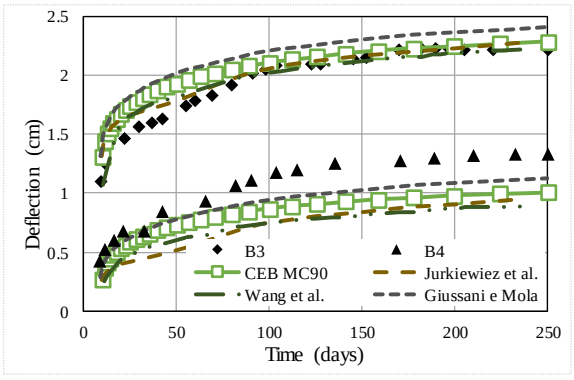

(d) CEB-MC90 model

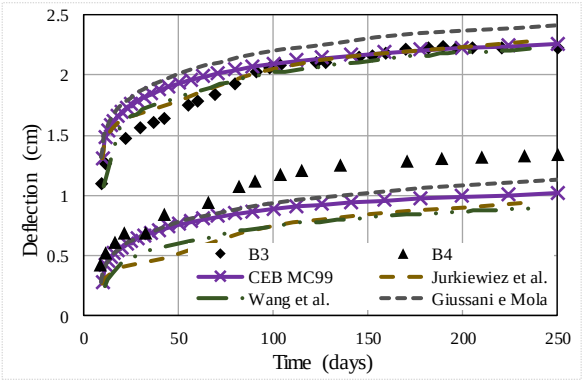

(e) CEB-MC99 model

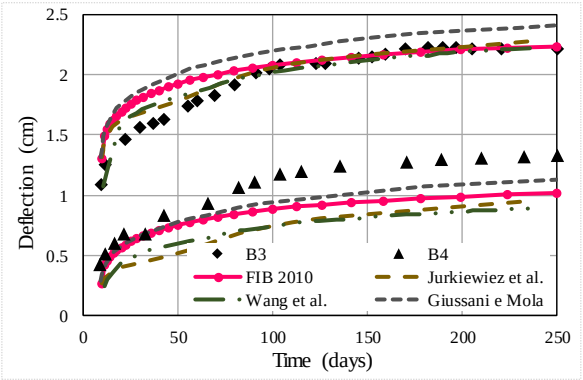

(f) FIB 2010 model

Fig. 8 Theoretical and experimental mid-span long-term deflection for beams B3/B4

Table 6 Statistical indicator for deflection at mid-span in continuous beam B1

Model	RD_{EXP} (%)	RD_{100p} (%)	ω_{BP} (%)	V_{CEB} (%)	F_{CEB} (%)	M_{CEB}	ω_G (%)
ACI 209	19.65	14.92	24.97	35.98	36.25	0.90	18.27
Bazant B3	14.09	6.43	17.77	32.33	32.58	0.81	12.18
GL2000	15.08	12.84	25.11	34.67	34.72	0.76	15.69
CEB MC90	18.58	23.67	30.24	37.50	37.26	0.73	18.67
CEB MC99	14.65	12.23	22.34	34.68	34.93	0.77	14.37
FIB 2010	14.92	12.19	22.47	34.75	35.01	0.77	14.55

Table 7 Statistical indicator for deflection at mid-span in continuous beam B2

Model	RD_{EXP} (%)	RD_{100p} (%)	ω_{BP} (%)	V_{CEB} (%)	F_{CEB} (%)	M_{CEB}	ω_G (%)
ACI 209	13.69	14.25	16.38	17.36	17.12	1.10	12.63
Bazant B3	9.35	11.22	12.61	12.97	12.91	1.06	9.29
GL2000	7.87	10.98	12.84	13.24	13.13	1.08	8.96
CEB MC90	8.01	9.38	11.48	11.91	11.84	1.06	8.45
CEB MC99	8.56	10.89	12.67	13.17	13.02	1.08	9.13
FIB 2010	7.91	10.29	12.14	12.57	12.46	1.07	8.70

RD_{EXP} indicator for beam B2. This is because the quoted coefficient is not able to deal with sparse data.

4.3 Steel-concrete composite beams tested by Fan et al. (2010)

In Fan *et al.* (2010) four steel-concrete composite beams subjected to positive and negative moments are tested under sustained load for a period of three years (1085 days). Two of them, namely LCB1 and LCB2, are cast with concrete grade C20 and C30, respectively, and subjected to positive

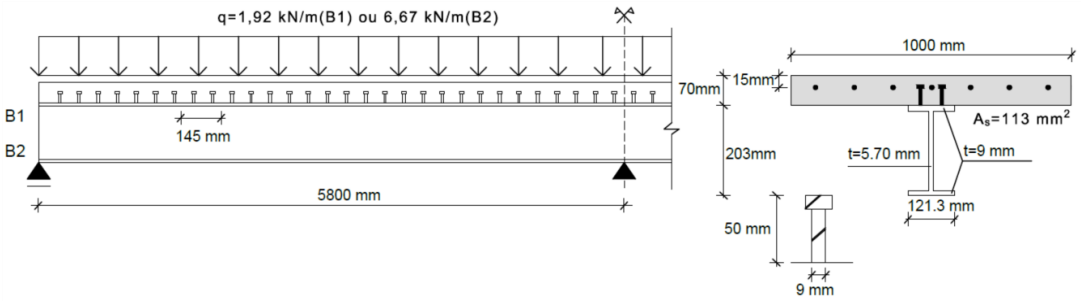

Fig. 9 Geometry and cross-section of continuous beams B1 and B2

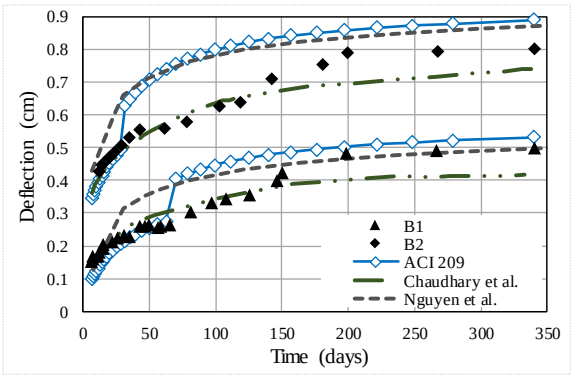

(a) ACI 209 model

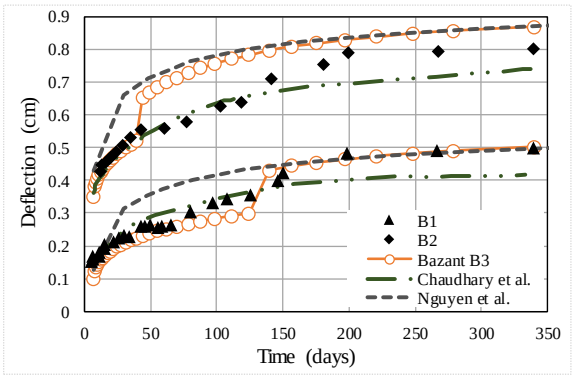

(b) Bazant B3 model

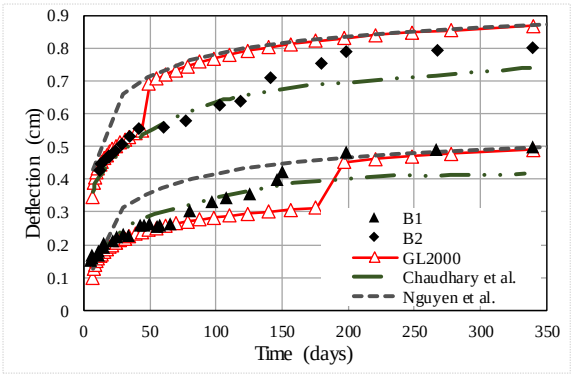

(c) GL 2000 model

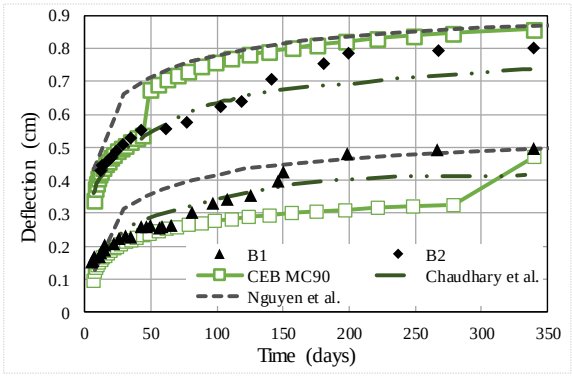

(d) CEB-MC90 model

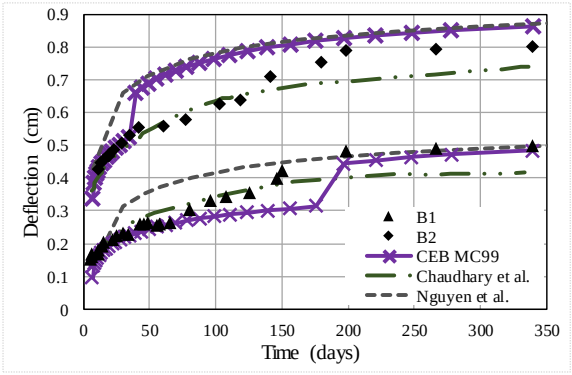

(e) CEB-MC99 model

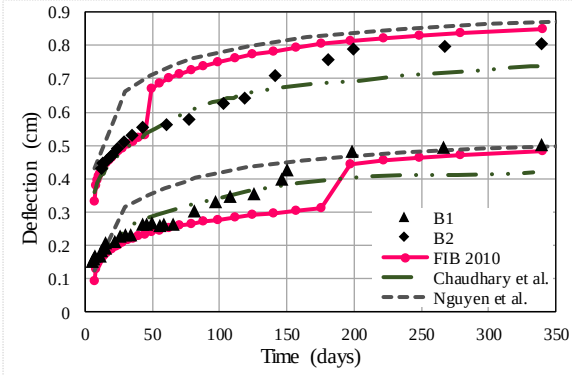

(f) FIB 2010 model

Fig. 10 Theoretical and experimental mid-span long-term deflection for continuous beams B1/B2

bending moments, while the other two, namely LCB3 and LCB4, have different steel ratios, concrete grade C30 and subjected to negative bending moments. A sketch of the cross section and beam geometry is shown in Figs. 11-12. The welded shear studs are 10 mm in diameter and 45 mm in height, and they are spaced at even intervals of 150 mm for beam LCB3 and 80 mm for the other three. Simply supported beams LCB1 and LCB2 are submitted to a distributed uniform load of 7.29 kN/m including self-weight, whereas beams LCB3 and LCB4, with an interior

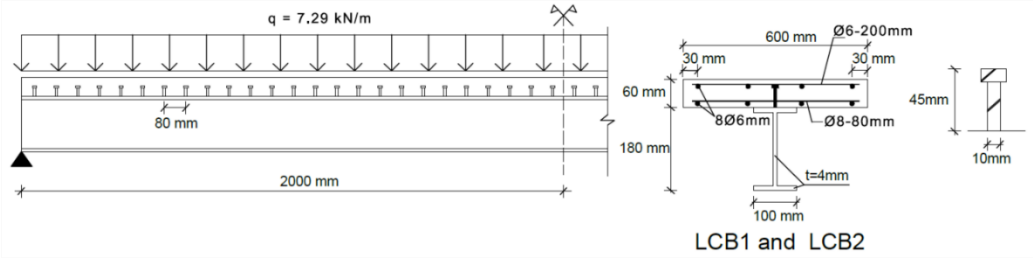

Fig. 11 Geometry and cross-section of beams LCB1 and LCB2

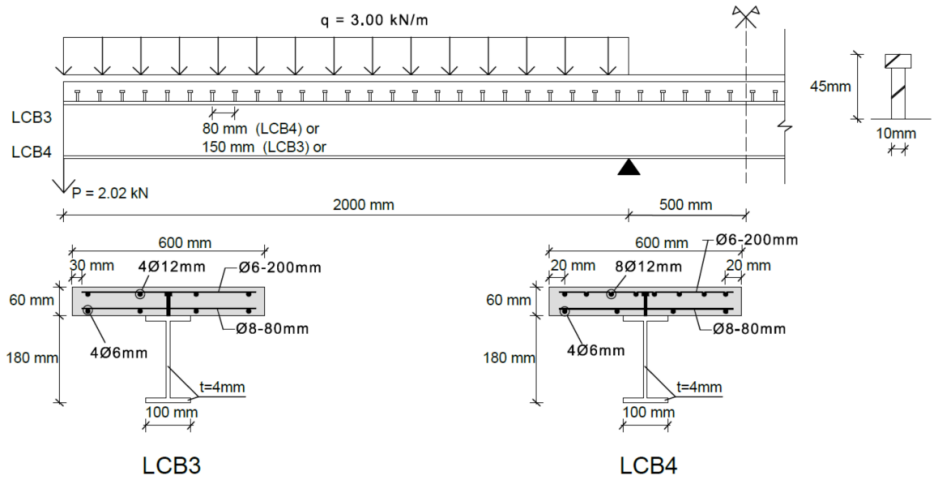

Fig. 12 Geometry and cross-section of beams LCB3 and LCB4

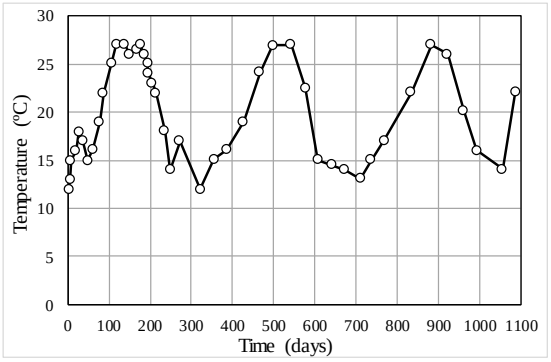

(a) Temperature

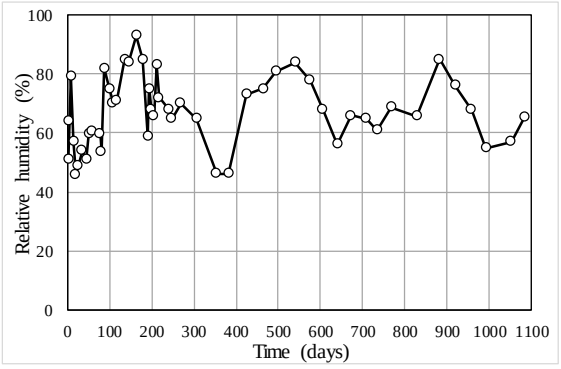

(b) Relative humidity

Fig. 13 Test environmental conditions in time

span and two cantilevers, are submitted to point loads of 2.02 kN at their free ends and to a distributed load of 3.0 kN/m at the cantilever spans. These applied loads generate negative flexure at the interior span and continuity of flexural moments at the supports, similar to those encountered in a practical bridge structure.

The ages of loading and curing time of the specimen beams are 7 days. Environmental conditions measured during the test are depicted in Fig. 13. In a first approach, as in the previous examples, the ultimate shrinkage strain is attained by a fitting procedure, while in a second approach current environmental quantities as depicted in Fig. 13 are employed in the numerical computations. Free-shrinkage strains at three parallepiped specimens were measured in the lab under the same environmental conditions of the specimen beams, and their average values are displayed in Figs. 14-15. Also, in the same figures are depicted the prediction of free shrinkage strains using the two aforementioned approaches for concrete grades C20 and C30. As it may be observed, the ultimate shrinkage strain is clearly attained in Fig. 14 as requested. In contrast, only the GL2000 model reaches spontaneously the experimental ultimate shrinkage strain in Fig. 15(a), while in other cases, shrinkage strains are clearly underestimated mainly for concrete grade C30 as shown in Fig. 15(b).

In Fig. 16 are depicted the time-history evolution of deflections at some monitoring points, e.g., mid- and quarter-span for beams LCB1, LCB2 and free ends for beams LCB3 and LCB4. The results correspond to the case of adjusted ultimate shrinkage strain. As it may be observed, the predicted deflections do not oscillate with time and they are in general overestimated. In Fig. 17 are depicted the same results, but with current environmental conditions. As it may be observed, predicted values are in

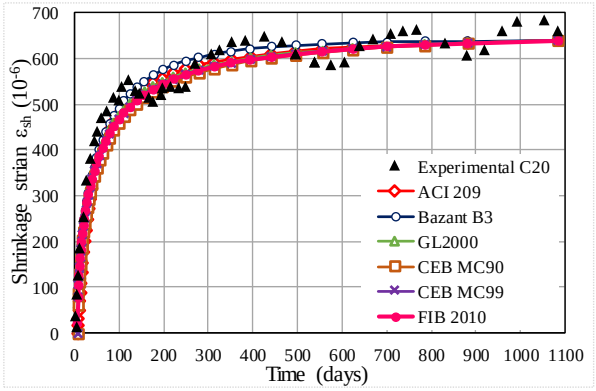

(a) C20 Concrete

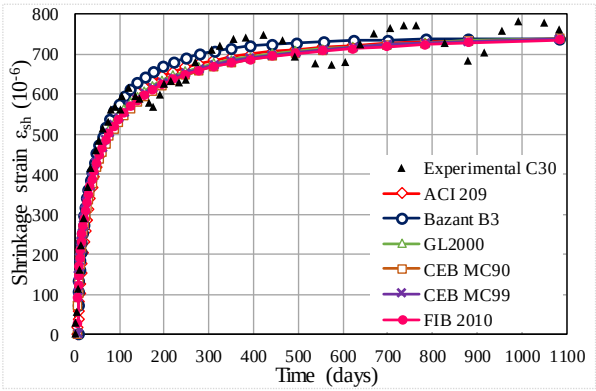

(b) C30 Concrete

Fig. 14 Free-shrinkage strain: adjusted ultimate shrinkage strain for rheological models

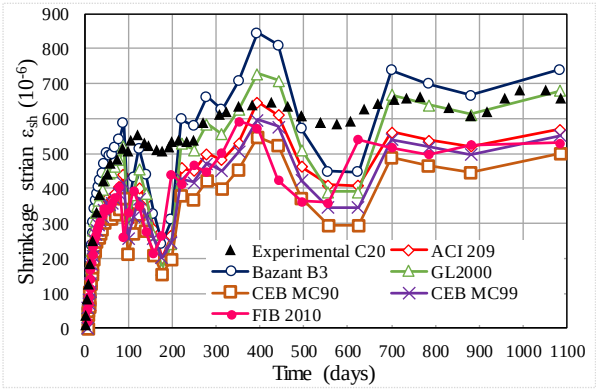

(a) C20 Concrete

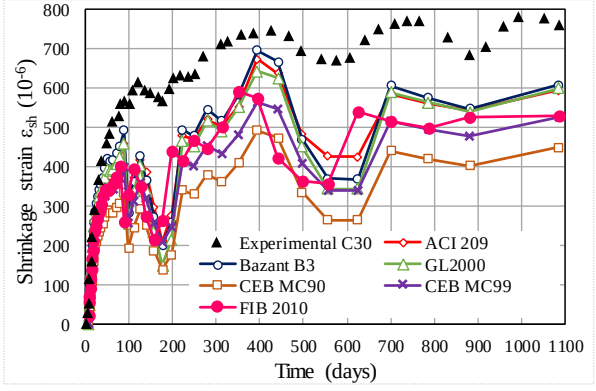

(b) C30 Concrete

Fig. 15 Free-shrinkage strain: variable environmental conditions for rheological models

Table 8 Statistical indicator for deflection at mid-span in continuous beam LCB1

Model	RD_{EXP} (%)	RD_{100p} (%)	ω_{BP} (%)	V_{CEB} (%)	F_{CEB} (%)	M_{CEB}	ω_G (%)
Adjusted shrinkage							
ACI 209	11.56	11.59	18.99	33.70	37.89	0.96	16.76
B3	9.59	10.03	17.52	32.33	36.78	0.97	14.48
GL2000	9.58	10.06	17.81	32.38	36.87	0.98	14.56
CEB MC90	8.97	9.20	17.66	32.70	37.16	0.96	14.69
CEB MC99	9.18	9.68	17.71	32.52	37.05	0.97	14.40
FIB 2010	10.04	11.74	18.64	32.65	37.10	1.00	15.85
Variable conditions							
ACI 209	8.92	5.84	17.30	33.09	37.32	0.89	14.76
Bazant B3	13.54	13.78	21.65	33.89	38.08	0.98	20.93
GL2000	11.53	10.58	19.41	32.96	37.34	0.95	18.21
CEB MC90	11.27	7.51	18.00	33.60	37.86	0.84	15.75
CEB MC99	8.57	5.81	16.87	32.53	37.00	0.88	13.84
FIB 2010	7.04	4.89	15.97	31.58	36.12	0.91	12.19

Table 9 Statistical indicator for deflection at mid-span in continuous beam LCB2

Model	RD_{EXP} (%)	RD_{100p} (%)	ω_{BP} (%)	V_{CEB} (%)	F_{CEB} (%)	M_{CEB}	ω_G (%)
Adjusted shrinkage							
ACI 209	18.18	19.40	20.33	23.79	24.99	1.07	19.81
Bazant B3	19.20	20.11	20.35	23.67	24.90	1.10	21.15
GL2000	15.97	16.44	17.93	21.59	23.05	1.08	18.21
CEB MC90	15.33	16.39	18.00	21.62	23.08	1.06	17.25
CEB MC99	15.65	16.70	18.19	21.75	23.21	1.07	17.73
FIB 2010	17.15	18.31	19.29	22.31	23.67	1.09	19.37
Variable conditions							
ACI 209	8.18	5.61	12.42	18.19	19.69	0.94	10.38
Bazant B3	8.99	7.12	12.26	17.48	19.07	0.96	11.09
GL2000	8.69	6.57	12.30	17.55	19.21	0.95	10.95
CEB MC90	14.14	11.59	15.35	20.78	22.14	0.85	15.57
CEB MC99	8.56	5.93	11.92	17.83	19.47	0.90	9.62
FIB 2010	9.54	8.56	13.19	17.61	19.20	1.00	12.85

close agreement with experimental values for beams LCB1 and LCB2 and the numerical solution is able to reproduce the oscillation pattern of the data. In case of beams LCB3 and LCB4, the oscillation is also captured, but the results are considerably more disperse and differentiated. In most situations, the predicted results are on the safe side.

In Tables 8-11 are listed the statistical indicators for both approaches. In the fitted case, the best result is obtained for the B3 model for beam LCB1, meanwhile the GL2000 model excels for the other three beams. For variable environmental conditions, the FIB 2010 outperforms the others for beam LCB1, while CEB MC 99 better behaves in the case of beam LCB3. Otherwise, models B3 and CEB MC 90 better performance for beams LCB2 and LCB4, respectively.

4.4 Effect of ultimate tensile strain, environmental humidity and temperature

In this section, the ultimate tensile concrete strain ε_{tu},

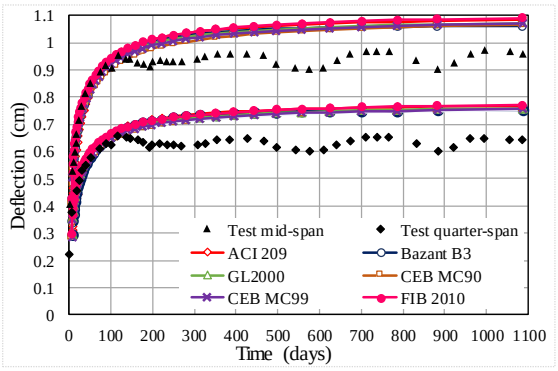

(a) LCB1 beam

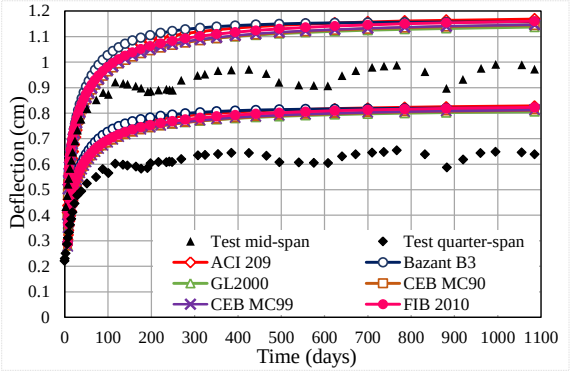

(b) LCB2 beam

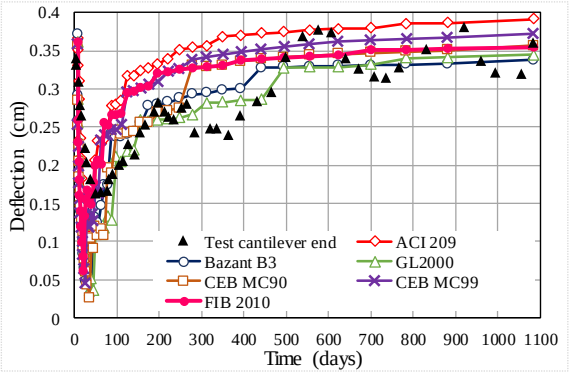

(c) LCB3 beam

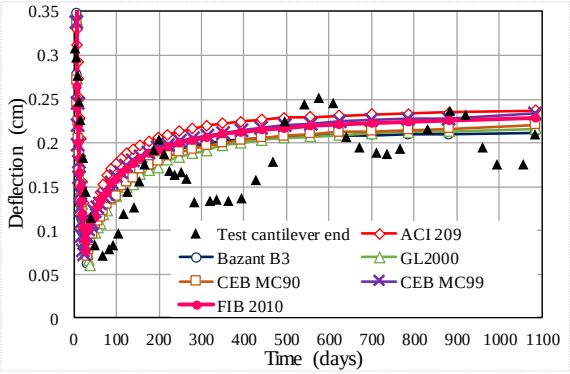

(d) LCB4 beam

Fig. 16 Experimental values and numerical deflections with adjusted shrinkage.

Table 10 Statistical indicator for deflection at free end of continuous beam LCB3

Model	RD_{EXP} (%)	RD_{100p} (%)	ω_{BP} (%)	V_{CEB} (%)	F_{CEB} (%)	M_{CEB}	ω_G (%)
Adjusted shrinkage							
ACI 209	27.37	22.37	27.01	31.61	32.57	1.09	32.15
Bazant B3	16.08	10.54	25.17	29.85	28.72	0.90	26.57
GL2000	14.57	9.18	24.42	28.18	27.42	0.86	24.71
CEB MC90	17.07	12.91	25.06	29.07	28.12	0.92	26.59
CEB MC99	23.57	17.40	27.90	32.66	31.61	1.01	31.57
FIB 2010	22.17	15.74	25.92	30.40	29.59	1.00	28.71
Variable conditions							
ACI 209	56.38	62.08	55.08	58.13	59.24	1.34	59.40
Bazant B3	54.02	58.52	52.64	56.55	57.19	1.27	58.81
GL2000	32.64	28.12	30.51	37.67	38.33	0.90	36.57
CEB MC90	29.46	29.20	32.68	34.88	35.06	0.75	36.39
CEB MC99	28.07	23.44	28.71	34.64	35.47	0.88	36.97
FIB 2010	30.88	25.94	30.77	37.14	36.56	1.05	36.91

Table 11 Statistical indicator for deflection at free end of continuous beam LCB4

Model	RD_{EXP} (%)	RD_{100p} (%)	ω_{BP} (%)	V_{CEB} (%)	F_{CEB} (%)	M_{CEB}	ω_G (%)
Adjusted shrinkage							
ACI 209	33.30	28.59	38.43	37.89	46.97	1.17	39.76
Bazant B3	25.59	20.50	35.13	34.13	38.11	1.04	34.79
GL2000	22.68	18.66	34.54	31.85	34.45	1.01	32.72
CEB MC90	24.01	19.87	35.33	32.98	35.81	1.03	34.26
CEB MC99	29.77	24.80	38.12	37.77	42.17	1.09	40.31
FIB 2010	28.29	23.63	35.99	35.24	40.75	1.09	37.43
Variable conditions							
ACI 209	74.06	76.56	62.39	71.12	77.77	1.50	69.93
Bazant B3	74.94	76.59	61.42	72.17	78.65	1.48	70.52
GL2000	40.62	39.88	41.98	47.04	50.37	1.21	45.05
CEB MC90	26.47	20.97	34.70	33.74	35.75	1.03	30.82
CEB MC99	34.14	32.51	39.43	41.01	44.35	1.15	41.80
FIB 2010	29.88	23.90	36.84	38.90	42.37	1.12	38.91

which can be considered a measure of tension stiffening, is varied to assess its effects on the long-term displacements of composite beams B1 and LCB3 from section 4.2 and 4.3, respectively, by using the FIB 2010 model. Although cracking is possible in simply supported composite beams, these beams are preferred because they are subjected to negative flexure. Ultimate tensile strains are mainly expressed in the range of 10 to 1000 times the cracking strain ε_{cr} as shown in Figs. 18(a), (b) for the long-term displacement evolutions of beams B1 and LCB3, respectively. It can be seen that values between $(20-30)\ \varepsilon_{cr}$ acceptable match the experimental response. The particular case for ε_{tu}=1.5ε_{cr} can be understood as the case in which tension stiffening is ignored, while ε_{tu}= 1000ε_{cr} means that the beam behaves like a beam with an uncracked slab. Thus, the way in which tension stiffening is included in the model significantly affects the response. A value of ε_{tu} =10 ε_{cr} excessively overestimates the deflection for beam LCB3.

In Fig. 18(c)-(d) is depicted the effect of the environmental humidity and temperature on the mid-span deflection of beam B1 for a fixed value of $\varepsilon_{tu} = 25\varepsilon_{cr}$. A

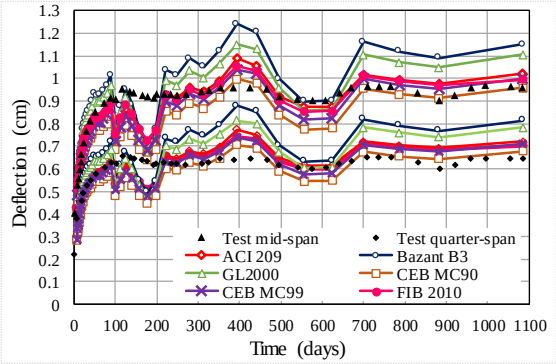

(a) LCB1 beam

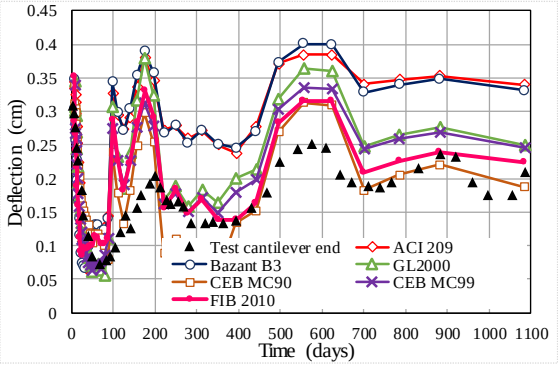

(b) LCB2 beam

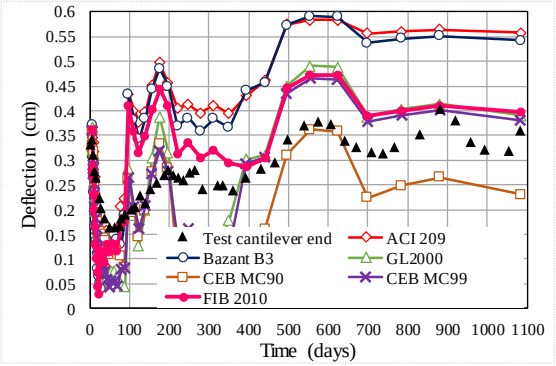

(c) LCB3 beam

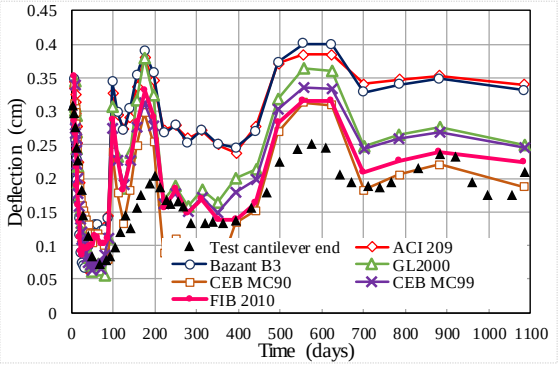

(d) LCB4 beam

Fig. 17 Experimental values and numerical deflections with variable environmental conditions

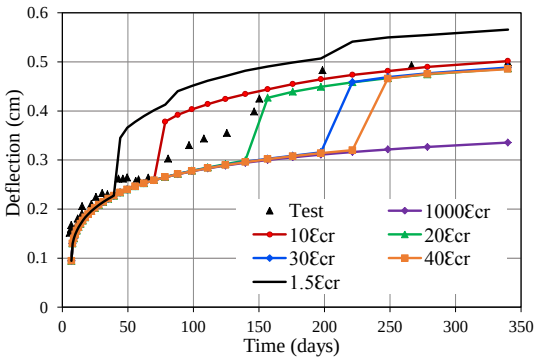

(a) Effect of ultimate tensile strain (beam B1)

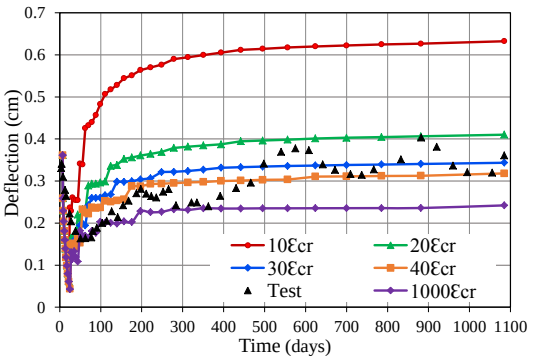

(b) Effect of ultimate tensile strain (beam LCB3)

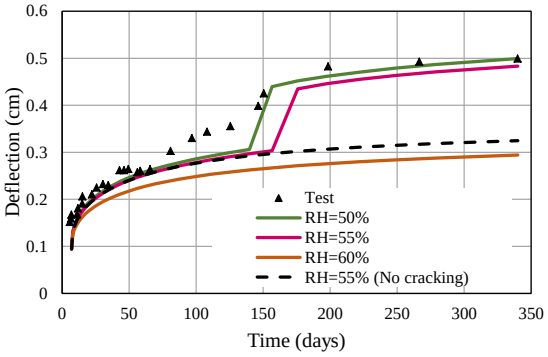

(c) Effect of environmental humidity (beam B1)

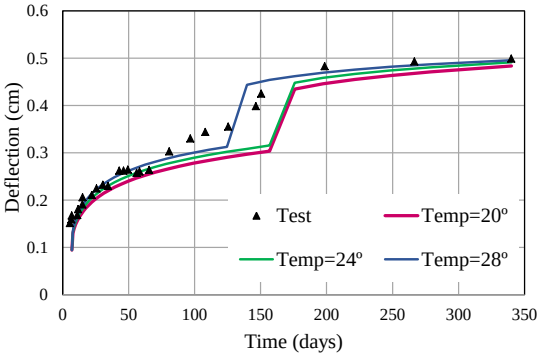

(d) Effect of temperature (beam B1)

Fig. 18 Mid-span and cantilever end displacements for beams B1 and LCB3.

coefficient of variation of 10% has been employed for the mean relative humidity of 55% in Fig. 18(c). As the environmental humidity increases the long-term deflection decreases because the shrinkage strain is reduced, e.g., the slab does not crack for a relative humidity of 60%. Conversely, in Fig. 18(d) the deflection slightly increases

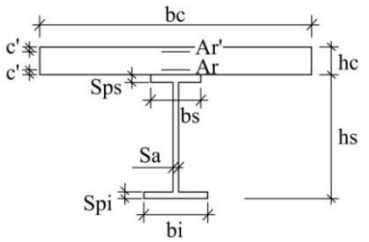

Steel profile			Concrete slab		
bs	=	600 mm	bc	=	6000 mm
bi	=	800 mm	hc	=	200 mm
Sps	=	60 mm	Ar'	=	6000 mm²
Spi	=	80 mm	Ar	=	6000 mm²
Sa	=	15 mm	c'	=	40 mm
hs	=	1600 mm			

Fig. 19 Geometry of the composite girder (Macorini *et al*. 2006)

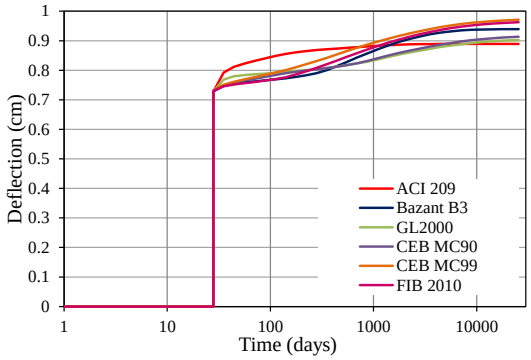

(a) Displacement at mid-span

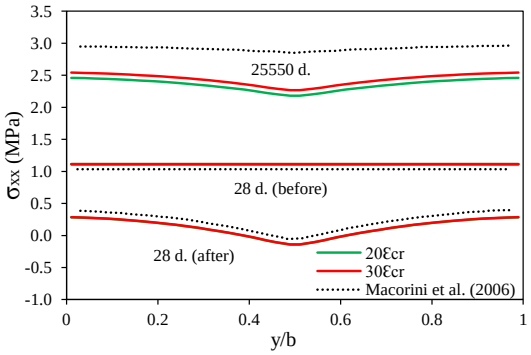

(b) Stress distribution at mid-span

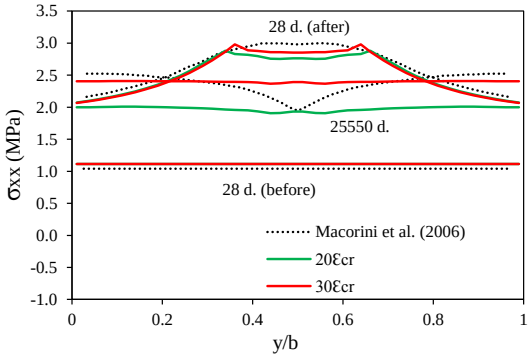

(c) Stress distribution at fixed end

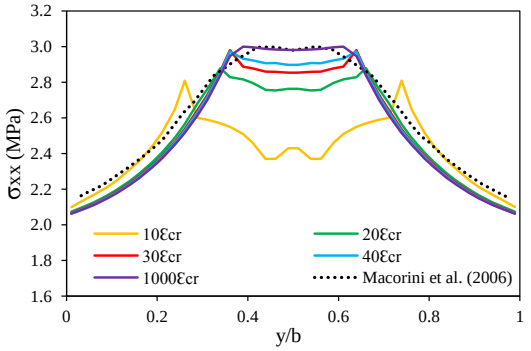

(d)Stress distribution in (c) immediately after 28 days

Fig. 20 History of displacement and stress distribution at the middle fiber of concrete slab

with temperature because the drying shrinkage is increased as the temperature is raised. The increasing of temperature generally reduces the amount of water which can be stored in the pore volume of the cement paste, resulting in the increase of drying shrinkage. Also, as the shrinkage increases, the slab cracks earlier as shown by the nearly vertical jump of curve with temperature of 28º.

4.5 Girder bridge studied by Macorini et al. (2006)

The proposed numerical model is used to investigate the composite beam studied by Macorini *et al.* (2006) subjected to long-term loading. The structure is a 25 m single span girder beam with fixed ends, representing an intermediate span of a continuous girder bridge. The geometric characteristic of the composite section are depicted in Fig. 19. The cylindrical compressive strength and the mean value of the tensile concrete strength are 35 MPa and 3.05 MPa, respectively. The relative humidity at which the structure is exposed is 75% with a notional member size of 193.5 mm. The connection system is considered to have a shear stiffness per unit length of 3.0 kN/mm^2, whereas the steel beam and the reinforcing bars have an elastic Young's modulus of 210000 MPa. Creep and shrinkage are evaluated according to the FIB 2010 model code, assuming that rheological phenomena begin from time of concrete hardening. This time is assumed to start 1 day after concrete casting, therefore it corresponds to the beginning of the time-history analysis. Thereafter, an external load (100 kN/m) is applied at 28 days and held constant afterwards for 25550 days (70 years). As generally occurs in bridges, unpropped construction is used.

Since the real concrete composition is unknown, the composition parameters are obtained based on a virtual mix design that will achieve the given concrete strength. Once these parameters are determined, the creep and shrinkage functions are defined for each rheological model. The displacement history at mid-span is depicted in Fig. 20(a), where the pre-loading stage in which shrinkage acts alone does not generate any meaningful displacement in the unpropped girder. The maximum and minimum long-term displacements after 25550 days are 0.97cm and 0.89 cm for

the CEB MC99 and ACI models, respectively. Nevertheless, retrained shrinkage induces stresses at the middle fiber of the concrete slab at the mid-span and fixed end as shown in Figs. 20(b)-(c), respectively. These initial tensile stresses named "curve 28 d. before", which stands for 28 days before load, are uniform across the dimensionless slab width at both sections with an approximately value of 1.0 MPa. This value almost represents one-third of the concrete tensile strength at 28 days (3.05 MPa). Then, it is expected that cracking will take place as soon as the external load is applied at 28 days. In Fig. 20(d) is shown the effect of the cracking strain on the stress distribution at the fixed end, immediately after the external load is applied at 28 days (curve 28 d. (after)).

As it may be observed, a value of ε_{tu}= $1000\varepsilon_{cr}$ better matches Macorini *et al.*'s stress distribution, but a value of ε_{tu}=$30\varepsilon_{cr}$ can be also used. It is important to mention that the results of the quoted work should be only taken as a reference and not as target. It can be inferred that the present stress distributions also illustrates the shear-lag variation with time.

5. Conclusions

In this work, the long-term deflection histories of ten steel-concrete composite beams with experimental results are analyzed via statistical bias indicators for some classical rheological models (ACI, CEB90, CEB99, B3, GL2000, and FIB2010). It can be stated that the ACI model better performance in case of the simply supported beams of section 4.1, but it does not perform well for other examples. For the two continuous composite beams of section 4.2, the B3 model outperforms the other models in average terms. Meanwhile, the GL2000 model better behave for the examples with negative and positive flexure of section 4.3 for the case of fitted ultimate shrinkage strain. However, when current variable environmental conditions are introduced, there is not a unique model that stands outs. The "best" rheological model in a given example does not necessarily imply that it succeeded in all statistical indicator values. Based on these findings, the following conclusions can be drawn.

- The statistical indicators ω_{BP}, V_{CEB}, F_{CEB} and ω_B better characterized the long-term prediction of deflections, allowing trace meaningful differences among all evaluated creep and shrinkage models. Conversely, the use of the M_{CEB} indicator hardly permits to distinguish between model performances.
- Input values for each concrete model, e.g., relative humidity, temperature and cement type, have been taken in order that the predicted shrinkage strain at ultimate time be nearly equal to the measure one, giving origin to the already mentioned fitting or adjusting procedure. Matching this parameter greatly reduces the dispersion between numerical and experimental results as shown for beams of section 4.3. In case of beams of section 4.1 and 4.2, this would be the natural approach because no information about environmental conditions and concrete mix components are provided. Even if the shrinkage evolution curve is available as occurs for beams of section 4.2, it cannot be strictly reproduced due to lack of other data. It is believed that the predicted deflections can be improved and corresponding statistical bias indicators, if the shrinkage strain could be adjusted at various points along time and not only at the end. However, this will further complicate the analysis because an assumed time-history for environmental conditions must be considered. To simplify the problem, nearly constant relative humidity and temperature are mainly used herein.
- Another key parameter that significantly influences the long-term predictions is the ultimate tensile strain. This parameter is problem dependent, but values in the range of $\varepsilon_{tu} \cong (20-30)\varepsilon_{cr}$, where ε_{tu} and ε_{cr} are the ultimate tensile and cracking strains, respectively, are found to yield acceptable results with the current tension stiffening model. Lower values will characterize excessive cracking in the slab, early interrupting the numerical convergence of the FE model. Otherwise, greater values could not capture the nearly vertical jumps exhibit in the experimental time history curves for negative flexure as substantiated in section 4.4.
- The highest errors committed in the prediction of the ultimate long-term deflection at mid-span in relation to the experimental one are: -2.6% (FIB 2010) and 3.4% (GL2000), respectively, for beams B1 and B3 of section 4.1. These errors are substantially increased up to -19.9% and -22.6% for beams B2 and B4 (CEB MC90), respectively. For the continuous beams of section 4.2, the associated maximum errors are 6.4% and 10.8% for beams B1 and B2, respectively (ACI 209 model). Moreover, the maximum errors associated to mid-span deflections of beams LCB1, LCB2, and cantilever end displacements of beams LCB3 and LCB4 of section 4.3 are 14% (FIB2010), 20.2% (ACI 209), 8.3% (ACI 209) and 12.9% (ACI 209), respectively. It is thus noted that even by adjusting the ultimate shrinkage strain; the error can be significant in some cases.
- Increasing the relative humidity and decreasing the ambient temperature can lead to a substantial reduction of slab cracking for beams under negative flexure. This is because shrinkage strain reduces under both situations.
- The correct inclusion of a pre-loading stage to take into account early shrinkage is relevant for the installation of initial tensile stresses in the concrete slab of a girder bridge as explained in section 4.5. This modifies the tension stiffening of the member and its cracking performance afterwards. However, for the studied experimental beams, the early shrinkage effect is considered to be diminished by the propped construction sequence and early testing.

Acknowledgments

The financial support provided by CAPES and CNPq is gratefully acknowledged.

References

ABAQUS (2011), Standard User's Manual, Version 6.11, Hibbit, Karlsson and Sorensen Inc, Pawtucket, RI, USA.

ACI Committee 209 (2008), Guide for Modeling and Calculating Shrinkage and Creep in Hardened Concrete, American Concrete Institute, Farmington Hills, MI, USA.

Ban, H., Uy, B., Pathirana, S.W., Henderson, I., Mirza, O. and Zhu, X. (2015), "Time-dependent behavior of composite beams with blind bolts under sustained loads", *J. Constr. Steel Res.*, **112**, 196-207. https://doi.org/10.1016/j.jcsr.2015.05.004.

Baskar, K., Shanmugam, N.E. and Thevendran, V. (2002), "Finite element analysis of steel-concrete composite plate girder", *J. Struct. Eng.*, **128**(9), 1158-1168. https://doi.org/10.1061/(ASCE)0733-9445(2002)128:9(1158).

Bazant, Z.P. and Bajewa, S. (1995), "Creep and shrinkage prediction model for analysis and design of concrete structures-Model B3", *Mater. Struct.*, **28**(180), 357-365. https://doi.org/10.1007/bf02473152.

Bazant, Z.P. and Li, G. (2008), "Unbiased statistical comparison of creep and shrinkage prediction models", *ACI Mater. J.*, **106**(6), 610-621.

Bazant, Z.P. and Panula, L. (1978), "Practical prediction of time dependent deformations of concrete, Part I," *Mater. Struct.*, **11**(5), 307-316. https://doi.org/10.1007/BF02473872.

Bazant, Z.P. and Prasannan, S. (1989), "Solidification theory for aging creep II: verification and application" *J. Eng. Mech.*, **115**(8), 1704-1725. https://doi.org/10.1061/(ASCE)0733-9399(1989)115:8(1691).

Bradford, M.A. and Gilbert, R.I. (1991), "Time-dependent behavior of simply-supported steel-concrete composite beams", *Mag. Concrete Res.*, **43**(157), 265-274. https://doi.org/10.1680/macr.1991.43.157.265.

Chaudhary, S., Pendharkar, U. and Nagpal, A.K. (2007). "Hybrid procedure for cracking and time-dependent effects in composite frames at service load", *J. Struct. Eng.*, ASCE, **133**(2), 166-175. https://doi.org/10.1061/(ASCE)0733-9445(2007)133:2(166).

Comité Euro-International du Béton CEB (1993), CEB-FIP Model Code 1990, CEB Bulletin d'Information No 213/214, Committee European du Béton-Fédération Internationale de la Précontrainte, Lausanne, Switzerland.

Comité Euro-International du Béton CEB (1999), Structural Concrete-Textbook on Behavior, Design and Performance, Updated Knowledge of the CEB-FIP Model code 1990, fib bulletin 2, V. 2, Fédération Internationale du Béton, Lausanne, Switzerland.

Damjanic, F. and Owen, D.R.J. (1984), "Practical considerations for modeling of post-cracking behavior for finite element analysis of reinforced concrete structures", *Proceedings of the International Conference on Computer-aided Analysis and Design of Concrete Structures*, Swansea, U.K.

Dias, M., Tamayo, J.L.P., Morsch, I.B. and Awruch, M.A. (2015), "Time dependent finite element analysis of steel-concrete composite beams considering partial interaction", *Comput. Concrete*, **15**(4), 687-707. https://doi.org/10.12989/cac.2015.15.4.687.

EC2 Standardization European Committee (2004), Eurocode 2 EN 1991-1-1 Design of Concrete Structures, Part 1-1: General Rules and Rules for Buildings, CEN, Brussels, Belgium.

Erkmen, R.E. and Bradford, M.A. (2011), "Time-dependent creep and shrinkage analysis of composite beams curved in plan", *Comput. Struct.*, **89**(1-2), 67-77. https://doi.org/10.1016/j.compstruc.2010.08.004.

Fan J., Nie, J., Li, Q. and Wang, H. (2010), "Long-term behavior of composite beams under positive and negative bending. I: Experimental study", *J. Struct. Eng.*, **136**(7), 849-857. https://doi.org/10.1061/(ASCE)ST.1943-541X.0000175.

Féderation International du Béton FIB (2012), FIB-2010 Model Code 2010, Bulletin 65, V. 1, Fédération Internationale du Béton, Lausanne, Switzerland.

Gadner, N.J. and Lockman, M.J. (2001), "Design provisions for drying shrinkage and creep of normal strength concrete", *ACI Mater. J.*, **98**(2), 159-167.

Gardner, N.J. (2004), "Comparison of prediction provisions for drying shrinkage and creep of bormal strength concretes", *Can. J. Civil Eng.*, **31**(5), 767-775. https://doi.org/10.1139/l04-046.

Gilbert, R.I. and Bradford, M.A. (1995), "Time-dependent behavior of continuous composite beams at service loads", *J. Struct. Eng.*, **121**(2), 319-327. https://doi.org/10.1061/(ASCE)0733-9445(1995)121:2(319).

Gilbert, R.I., Bradford, M.A., Gholamhoseine, A. and Chang, Z.T. (2012), "Effect of shrinkage on the long-term stresses and deformations of composite concrete slabs", *Eng. Struct.*, **40**, 9-19. https://doi.org/10.1016/j.engstruct.2012.02.016.

Giussani, F. and Mola, F. (2010), "Displacement method for the long-term analysis of steel-concrete composite beams with flexible connection", *J. Struct. Eng.*, **136**(3), 265-274. https://doi.org/10.1061/(ASCE)ST.1943-541X.0000109.

Jiang, M., Qiu, W. and Zhang, Z. (2009), "Time-dependent analysis of steel-concrete composite beams", *International Conference on Engineering Computation*, Hong Kong, China, May.

Jurkiewiez, B., Buzon, S. and Sieffert, J. G. (2005), "Incremental viscoelastic analysis of composite beams with partial interaction", *Comput. Struct.*, **83**(21-22), 1780-1791. https://doi.org/10.1016/j.compstruc.2005.02.021.

Kaklauskas, G., Gribniak, V., Bacinskas, D. and Vainiunas, P. (2009), "Shrinkage influence on tension stiffening in concrete members", *Eng. Struct.*, **31**(6), 1305-1312. https://doi.org/10.1016/j.engstruct.2008.10.007.

Liang, Q.Q., Uy, B., Bradford, M.A. and Ronagh, H.R. (2005), "Strength analysis of steel-concrete composite beams in combined bending and shear", *J. Struct. Eng.*, **131**(10), 1593-1600. https://doi.org/10.1061/(ASCE)0733-9445(2005)131:10(1593).

Liu, X., Bradford, M.A. and Erkmen E. (2013), "Time-dependent response of spatially curved steel-concrete composite members. I: Computational Modeling", *J. Struct. Eng.*, **139**(12), 1-11. https://doi.org/10.1061/(ASCE)ST.1943-541X.0000698.

Macorini, L, Fragiacomo, M., Amadio, C. and Izzuddin, B.A. (2006), "Long-term analysis of steel-concrete composite beams: FE modeling for effective width evaluation", *Eng. Struct.*, **28**(8), 1110-1121. https://doi.org/10.1016/j.engstruct.2005.12.002.

Moreno, J.C.A. (2016), "Numerical analysis of steel-concrete composite beams by the finite element method: models for the long-term effect and internal prestressing", M.Sc. Dissertation, Federal University of Rio Grande do Sul, Porto Alegre. (In Portuguese)

Moscoso, A.M., Tamayo, J.L.P. and Morsch, I.B. (2017), "Numerical simulation of external pre-stressed steel concrete composite beams", *Comput. Concrete*, **19**(2), 191-201. https://doi.org/10.12989/cac.2017.19.2.191.

Muller, H.S. and Hilsdorf (1990), Evaluation of the Time Dependent of Behavior of Concrete, Bulletin d'ínformation No 199, Committee Euro-International du Beton (CEB), Lausanne, Switzerland.

Nguyen, Q. and Hjiaj, M. (2016), "Nonlinear time-dependent behavior of composite steel-concrete beams", *J. Struct. Eng.*, **142**(5), 1-11. https://doi.org/10.1061/(ASCE)ST.1943-541X.0001432.

Partov, D. and Kantchev, V. (2011), "Level of creep sensitivity in composite steel-concrete composite beams according to ACI-209R-92 model, comparison with Eurocode-4 (CEB MC90-

99)", *Eng. Mech.*, **18**(2), 91-116.
Ramnavas, M.P., Patel, K.A., Chaudhary, S. and Nagpal, A.K. (2015), "Cracked span length beam element for service load analysis of steel-concrete composite bridges", *Comput. Struct.*, **157**, 201-208. https://doi.org/10.1016/j.compstruc.2015.05.024.
Reginato, L.H., Tamayo, J.L.P. and Morsch, I.B. (2018), "Finite element study of effective width in steel-concrete composite beams under long-term service loads", *Latin. Am. J. Solid. Struct.*, **15**(8), 1-25. http://dx.doi.org/10.1590/1679-78254599.
Rex, O.C. and Easterling, W.S. (2000), "Behavior and modeling of reinforced composite slab in tension", *J. Struct. Eng.*, **126**(7), 764-771. https://doi.org/10.1061/(ASCE)0733-9445(2000)126:7(764).
Sakr, M.A. and Sakla, S.S. (2008), "Long term deflection of cracked composite beams with nonlinear partial shear interaction: I-Finite element modeling", *J. Constr. Steel Res.*, **64**(12), 1446-1455. https://doi.org/10.1016/j.jcsr.2008.01.003.
Sousa, H., Bento, J. and Figueiras, J. (2013), "Construction assessment and long-term prediction of prestressed concrete bridges based on monitoring data", *Eng. Struct.*, **52**, 26-37. https://doi.org/10.1016/j.engstruct.2013.02.003.
Tamayo, J.L.P. and Awruch, M.A. (2016), "Numerical simulation of reinforced concrete nuclear containment under extreme loads", *Struct. Eng. Mech.*, **58**(5), 799-823. https://doi.org/10.12989/sem.2016.58.5.799.
Tamayo, J.L.P., Franco, M.I., Morsch, I.B., Désir, J.M. and Wayar, A.M. (2019), "Some aspects of numerical modeling of steel-concrete composite beams with prestressed tendons", *Latin. Am. J. Solid. Struct.*, **16**(7), 1-19. http://dx.doi.org/10.1590/1679-78255599.
Tamayo, J.L.P., Morsch, I.B. and Awruch, M.A. (2015), "Short-time numerical analysis of steel-concrete composite beams", *J. Braz. Soc. Mech. Sci. Eng.*, **37**(4), 1097-1109. https://doi.org/10.1007/s40430-014-0237-9.
Theiner, Y., Andreatta, A. and Hofstetter, G. (2014), "Evaluation of models for estimating concrete strains due to drying shrinkage", *Struct. Concrete*, **15**(4), 461-468. https://doi.org/10.1002/suco.201300082.
Varshney, L.K., Patel, K.A., Chaudhary, S. and Nagpal, A.K. (2013), "Control of time-dependent effects in steel-concrete composite frames", *Int. J. Steel Struct.*, **13**(4), 589-606. https://doi.org/10.1007/s13296-013-4002-1.
Wang, W.W., Dai, J.G., Li, G. and Huang, C.K. (2011), "Long-term behavior of prestressed old-new concrete composite beams", *J. Bridge Eng.*, **16**(2), 275-285. https://doi.org/10.1061/(ASCE)BE.1943-5592.0000152.
Wendner, R., Hubler, M.H. and Bazant, Z.P. (2015), "Optimization method, choice of form and uncertainty quantification of model B4 using laboratory and multi-decade bridge databases", *Mater. Struct.*, **48**(4), 771-796. https://doi.org/10.1617/s11527-014-0515-0.
Xiang, T., Yang, C. and Zhao, G. (2016), "Stochastic creep and shrinkage effect of steel-concrete composite beam", *Adv. Struct. Eng.*, **18**(8), 1129-1140. https://doi.org/10.1260/1369-4332.18.8.1129.
Xu, L., Nie, X. and Tao, M. (2018), "Rotational modeling for cracking behavior of RC slabs in composite beams subjected to a hogging moment", *Constr. Build. Mater.*, **192**, 357-365. https://doi.org/10.1016/j.conbuildmat.2018.10.163.
Zhu, L. and Su, R.K.L. (2017), "Analytical solutions for composite beams with slip, shear-lag and time-dependent effects", *Eng. Struct.*, **152**, 559-578. https://doi.org/10.1016/j.engstruct.2017.08.071.